CHALMERS
UNIVERSITY OF TECHNOLOGY

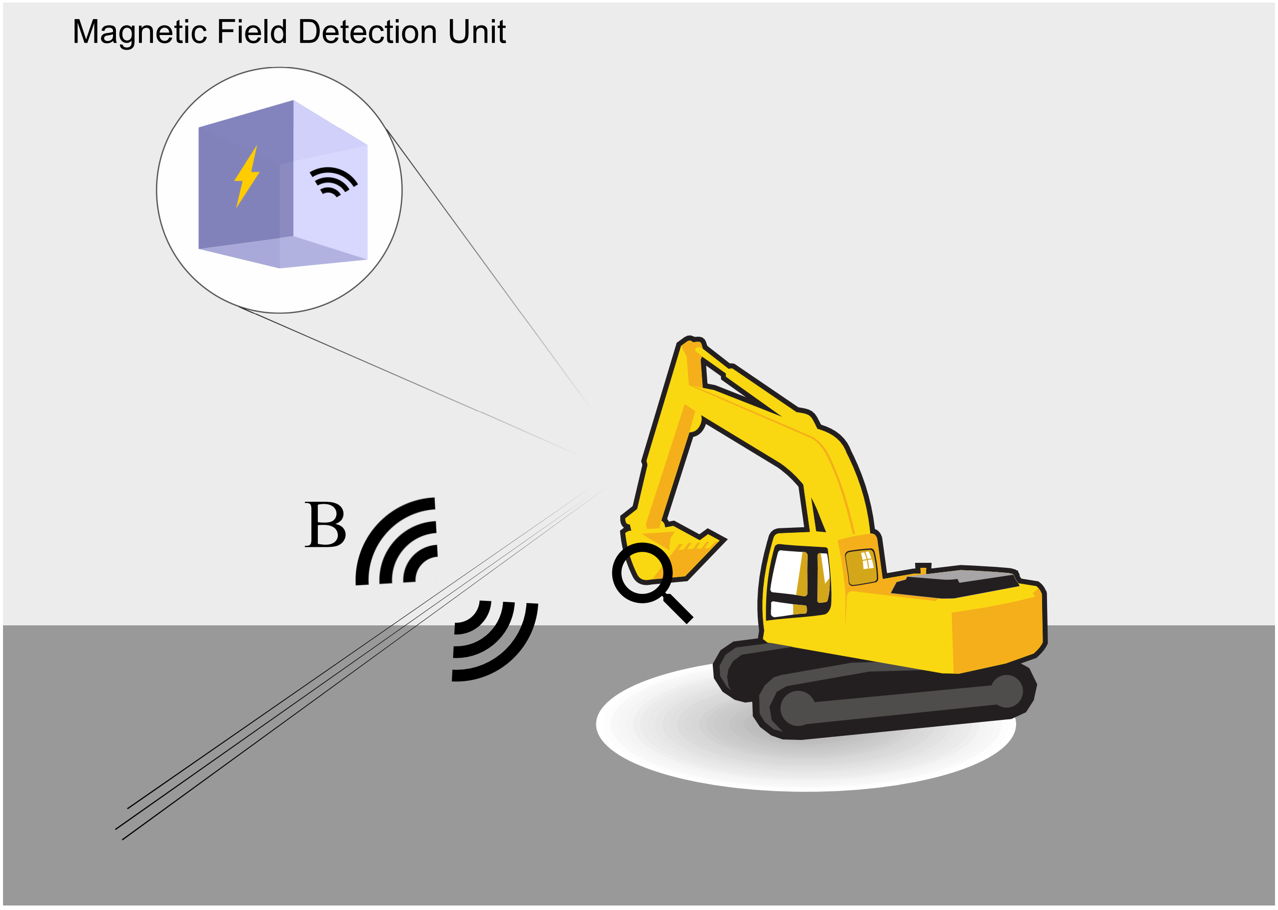

Detection of high-voltage power cables using electromagnetic sensing equipment on an excavator

Master's thesis in Embedded Electronic System Design

Carl-Johan Häll
Otto Torgnyson

Department of Computer Science and Engineering
CHALMERS UNIVERSITY OF TECHNOLOGY
Gothenburg, Sweden 2015

Master's thesis 2015:08

Detection of high-voltage power cables using electromagnetic sensing equipment on an excavator

Carl-Johan Häll

Otto Torgnyson

CHALMERS
UNIVERSITY OF TECHNOLOGY

Department of Computer Science and Engineering
Division of Computer Engineering
Chalmers University of Technology
Gothenburg, Sweden 2015

Detection of high-voltage power cables using electromagnetic sensing equipment on an excavator

Carl-Johan Häll

Otto Torgnyson

Supervisor: Christian Eggertsen, CPAC Systems AB and Arne Linde, Chalmers University of Technology
Examiner: Per Larsson-Edefors, Department of Computer Science and Engineering, Chalmers University of Technology

Master's Thesis 2015:08
Department of Computer Science and Engineering
Division of Computer Engineering
Chalmers University of Technology
SE-412 96 Gothenburg
Telephone +46 31 772 1000

Cover: A scenario where a cable detection unit detects a dug down power cable.

Typeset in LaTeX
Printed by TeknologTryck
Gothenburg, Sweden 2015

Detection of high-voltage power cables using electromagnetic sensing equipment on an excavator
Carl-Johan Häll
Otto Torgnyson
Department of Computer Science and Engineering
Chalmers University of Technology

Abstract

Detection of underground power cables and their location is possible with the help of high quality sensors and a fine electronic signal chain combined with advanced detection algorithms. By designing a sensor solution capable to capture 0.1 μT of magnetic flux density it is possible for an algorithm to pinpoint the location and current of the conductors in the ground. In a lab environment the placement error was measured to 15 cm with a 13 A (RMS) current. The product developed in this thesis can help to create a safer, more accurate and easy to use method for detection of underground power cables.

Keywords: Passive electromagnetic sensing, Magnetic field detection, MEMS, PCB design, Biologically inspired stochastic optimization, AMR.

Acknowledgements

We would like to express our gratitude to CPAC Systems AB for the opportunity to develop this thesis.

Furthermore this thesis improved from what it would elsewise had been with the help of some people that should be mentioned. We would like to thank the following:

Johan Nilsson, Peter Siljehov and Bo Larsson for the guidance and their expertise on how to make a successful hardware design.

Carl-Johan Häll and Otto Torgnyson, Gothenburg, August 2015

Acronyms

ADC Analog-to-Digital converter.

AIS Artifical immune system.

AMR Anisotropic magnetoresistive.

CAN Controller Area Network.

CDU Cable Detection Unit.

CMRR Common-mode rejection ratio.

CSR Current source reconstruction.

DSP Digital signal processing.

ECU Electric control unit.

EMF Electromagnetic field.

ENOB Effective number of bits.

FFT Fast fourier transform.

GA Genetic algorithm.

GMR Giant magnetoresistive.

IC Integrated circuit.

LDO Low Drop-Out.

LSB Least Significant Bit.

MCU Microcontroller unit.

MEMS Microelectromechanical systems.

MFD Magnetic flux density.

MFS Mean field strength.

PCB Printed circuit board.

PGA Programmable gain amplifier.

PSU Power supply unit.

RMS Root mean square.

SINAD Signal-to-noise and distortion ratio.

SNR Signal-to-Noise Ratio.

SoC System-on-a-Chip.

UART Universal asynchronous receiver/transmitter.

XLPE Cross-linked polyethylene.

Contents

List of Figures

List of Tables

1
Introduction

1.1 Background

Development and manufacturing of magnetometer solutions has enabled development of magnetometers of very small scale and high sensitivity [10]. A small scale solution allows more flexible placement and the increased sensitivity allows the measuring of physical quantities in a more delicate way.

In urban areas all around the world high voltage cables are buried underground and in many cases the knowledge regarding the exact locations of the cables are unknown to construction workers and engineers. To avoid damage on infrastructure, and the possibility of power interruption, power cables need to be detected before excavation starts on site. By integrating the feature of detection on the excavator arm, instead of using standalone handheld solutions, this can lead to increased efficiency of the excavation by reducing the number of steps in the process.

By using an integrated solution for detecting underground power cables the operator which is the one requesting the information, will get the information directly without having to acquire extra machinery; machinery which in turn demands personnel with machine specific training. Using an integrated sensor with in-machine analysis, the operator can get the information seconds after it is requested, or warn if a cable is near.

Solutions for detecting underground power cables exist, but special training is needed [11]. A factor for companies operating excavators or other digging tools is cost. Special training is expensive and tools need to be in use to make the investment profitable. By creating a product connected to a comprehensible interface, the special training will not be needed which makes the product more competitive.

By evaluating technologies for an industrial use, we can find new areas of application. This thesis will be about discovering suitable components and technologies for excavating purposes regarding detection of high-voltage power cables, an application which with new development is possible to integrate at lower cost and with greater quality than ever before. By using magnetometer technology our aim is to reduce the immense cost and risk that are conveyed while performing infrastructural work in urban areas.

1.2 Purpose

A great amount of high-voltage power cables are dug down each year. The location of these cables are not always exact and may differ from available drawings. Many cables were dug down in the last century with only paper drawings available to show their exact positions. The uncertainty of the location of high-voltage power cables may pose great danger to the personnel on the ground and infrastructure. It is therefore important to avoid damaging the cables.

This thesis focuses on a passive measurement method measuring the Magnetic flux density (MFD) generated by dug down high-voltage power cables. The purpose of the thesis is to answer four questions.

- Is it possible to measure the field surrounding a three-phase cable accurately enough?
- How do you design a prototype with components that are suitable for meeting the measurement quality demands?
- How do you extract cable location from the measured data?
- How can the system be integrated with the rest of the sensor system?

1.3 Scope and limitations

In this project we will measure, analyse, characterise the magnetic field surrounding dug-down high-voltage power cables. Electric fields will not be considered. By using existing sensors which provide the bucket position of an excavator and to combine it with a measured magnetic field it should be possible to create a 2 or 3 dimensional orientation of the cable routing.

The prototype will be used as a proof of concept and the long term goal of the project is a system which can be mounted on the arm of an excavator and also has integration support with the vehicle's existing sensor bus.

This thesis will focus on the hardware and software needed to detect dug down high-voltage cables. Test and verification will be done with a test rig but simulated data will also be used to be able to start detection algorithm development at an earlier stage. Disturbance sources will be taken into account but no immense investigation of the sources of disturbance will be undertaken in this project. The project will not include a thorough analysis of the prototype placement.

The budget for this project is limited and the equipment which needs to be acquired is restricted to a few sensors, microprocessors, prototype development and test rig parts.

1.4 Method

To realise the scope of the thesis the project is the divided in a set of three phases, analysis, model development, and product development. The phases are constructed to enable a continuous development by having set semi-goals during the process.

1.4.1 Overview

The overview aims to give a graphical approach of the phases and semi-goals of the project. A schematic of the main three phases and their semi-goals can be seen in Figure 1.1.

The thesis structure aims to give a founding understanding of the subject in Chapter 2, presenting practical knowledge and technology applied in this thesis. The following chapters regarding hardware (Chapter 3) and software (Chapter 4) implementation details explain our decisions throughout the design process. The results of the thesis are presented in Chapter 5 and then discussed and concluded in Chapter 6 and Chapter 7.

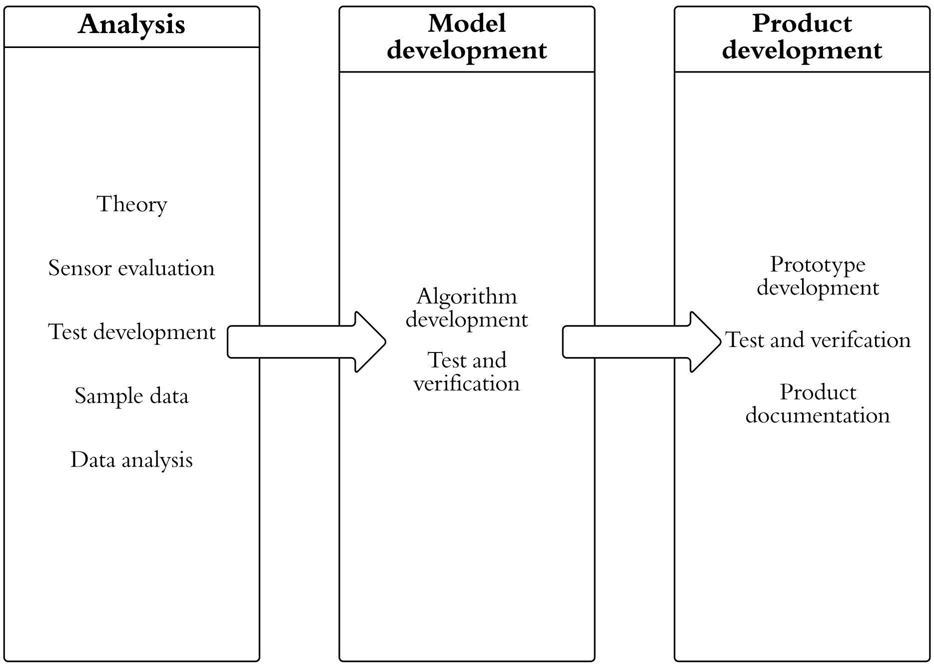

Figure 1.1: Phases of development

1.4.2 Analysis

In the first phase of the project, literature studies will be done to obtain a fundamental theoretical background. Some of the subjects to be investigated are sensor types, sensor specification, noise levels, magnetic flux characterization from cables, phase identification and frequency estimation.

When a theoretic background is established further evaluation of sensor specification and behaviour will be conducted. This evaluation specifies the sensor solutions to be used in the thesis for test and verification, data analysis and characterisation of the magnetic flux. Important properties for a magnetic flux sensor are the resolution, size, cost and range. The settled upon sensor solutions are then applied on a test-rig that emulates dug down cables conditions. The MFD surrounding the cable is measured and the approximated direction, depth, current and frequency is analysed. The test rig will both have to simulate sensor movement (the excavator arm will move) and the cable setup. For the data analysis we need to obtain measurements from different heights and different cable crossing angles for different cable setups.

The collected data will be analysed to check that it confirms theoretical models and proposed behavior. Signal processing may be needed to remove constant magnetic flux caused by the earth's magnetic field as well as other disturbance components.

1.4.3 Model development

A source identification algorithm will be developed based on the findings in the analysis. The outputs from this algorithm will be depth, direction, and current; all derived from the measured MFD of the cable at different points of measurement. This is to be done in a MATLAB/Simulink environment.

1.4.4 Product development

A great challenge with the prototype design lies in choosing the right platform. The prototype should be of small-size to enable placement on an excavator. Further it should have the ability to communicate with the sensor system which communicates with the Controller Area Network (CAN) protocol. The platform can be either an existing System-on-a-Chip (SoC) or a microprocessor placed on a custom Printed circuit board (PCB). The interfaces of the platform must be compatible for integration with the existing sensor network system [12].

This proof of concept is to be tested and verified with the test rig to verify its functionality. This verification will show the correctness of real-time data versus previously simulated behaviour. When these test results are at a satisfactory level the product can be further tested in a target scenario, mounted on the arm of an excavator.

2

Theory

For the analysis of sensors and design of the underground detection algorithm a deeper understanding of the theory is needed. The properties of the magnetic field surrounding a cable is presented in Section 2.1. Information regarding the power cables is mentioned in Section 2.2 where the orientation, current and formation is presented. The sensor technology is one of the most important aspects in this project and different technologies for measuring the MFD are presented in Section 2.3. The theory of extracting the cable orientation information out of measured values is based on inverse problem theory together with stochastic optimization techniques. These subjects are presented in Section 2.4 and Section 2.5.

2.1 Electromagnetic field theory

Electromagnetics is the study of the effects originating from electric charges, both in rest and in motion. Electromagnetic fields are present all around us and they have been used for centuries to navigate by compass and to communicate by TV/Radio. A field is a distribution of quantity in space and a time varying electric field is coupled with a time varying magnetic field, resulting in an Electromagnetic field (EMF). In this thesis focus will be on the MFD surrounding a typical underground high-voltage power cable [1].

2.1.1 Magnetic flux density

The symbol for the MFD is $\mathbf{B}$ and its unit is Tesla [T]. In this thesis measurements of the MFD surrounding a cable will be carried out. A good understanding of the theory is important to simulate the high-voltage power cables but also for creating cable models to be used in post-processing. A description of the geometry can be seen in Figure 2.1 below.

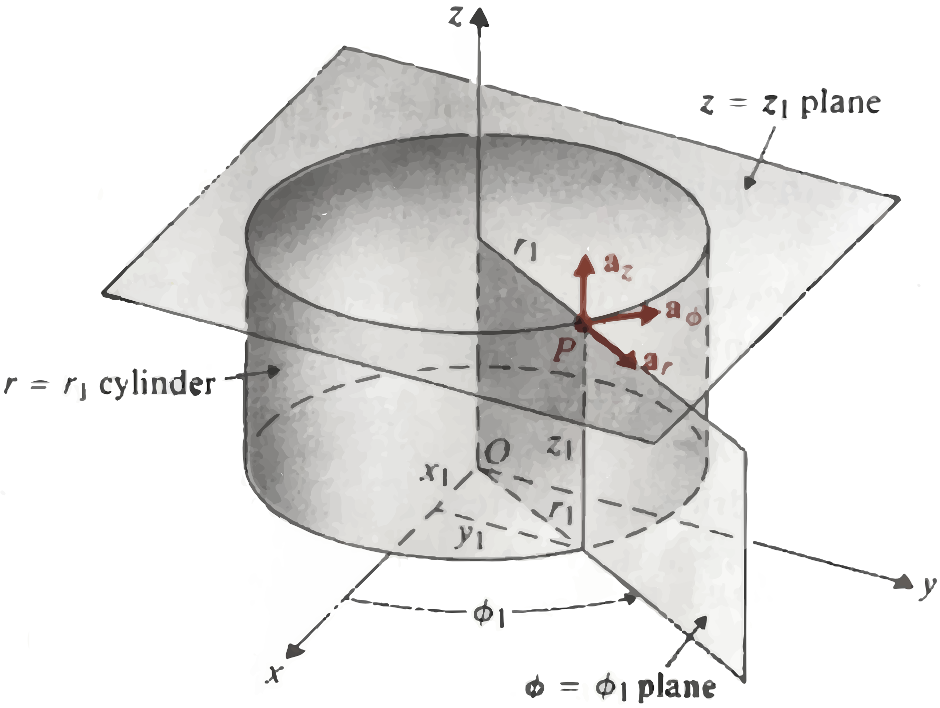

Figure 2.1: A figure describing the geometry along a line in cylindrical coordinates [1].

The cylindrical model can be used to model the geometry surrounding a cable. Under the assumption that the cable is completely straight, infinitely long and that there are no other nearby cables it can be said that the conductor is running in the z direction. With this model one can describe both the MFD inside a cable and at a distance from it. In Figure 2.2(a) a cross section of a cable and the $\mathbf{B}$ -field for different values of the radius is shown. The variable b marks the conductor radius.

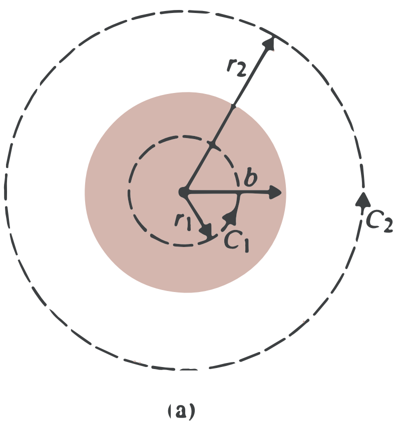

(a) Cross section view [1].

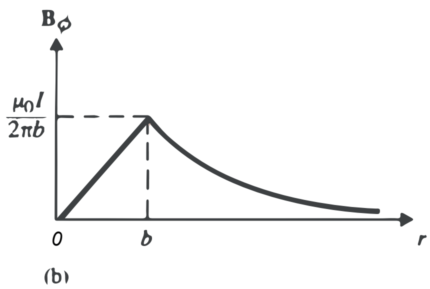

(b) MFD at different distances r [1].

Figure 2.2: Cross section of a conductor together with its MFD at different radiuses.

By looking at Figure 2.2(a) and Figure 2.2(b) one can see the impact on field reduction when moving between mediums. Inside the conductor the MFD will increase linearly and when the boundary condition $r > b$ occurs the point of measurement will move outside the conductor and the MFD will start to decrease. Since the measurements performed in this thesis will be remote, a deeper understanding of how to measure the MFD in air is needed. **B** for a single conductor is calculated by the following equation:

$$\mathbf{B} = a_\phi B_\phi = a_\phi \frac{\mu_0 I}{2\pi r} \tag{2.1}$$

Where μ_0 is the permeability constant, I is the current through the conductor and r is the radius from the center. The vector a_ϕ indicates that the direction of the field is perpendicular to the radius and the MFD will be the same for all ϕ. The $\frac{1}{r}$-factor explains the relation in Figure 2.2(b). In Figure 2.3 the relation between B_ϕ and r is plotted. To measure B_ϕ from such a conductor at a distance of 1 m demands that the measurement equipment is able to detect μT size fields. The values in Figure 2.3 are calculated from Eq. 2.1.

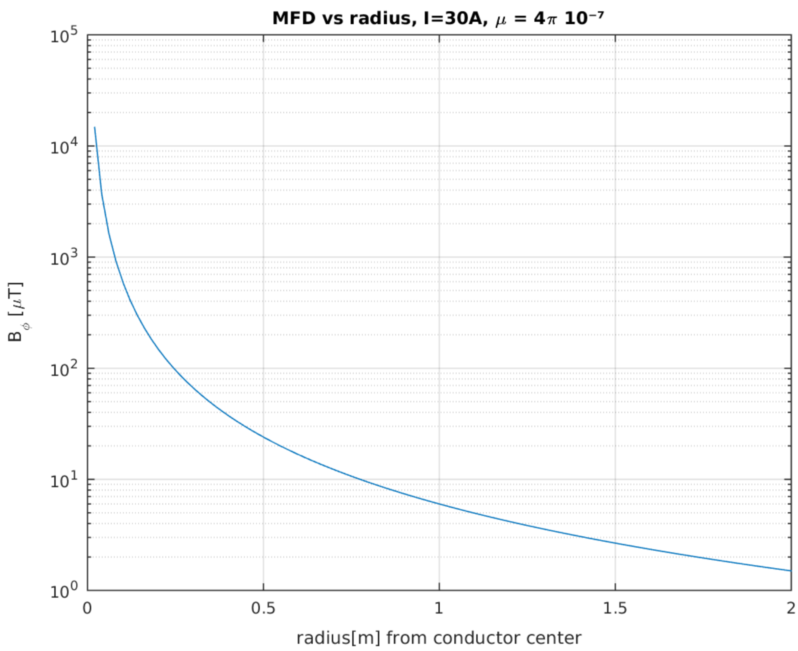

Figure 2.3: B_ϕ calculated using Eq. 2.1 for a 30 A current going through a 10 mm^2 infinitely long conductor.

Figure 2.4 shows a surface plot of how the MFD around a conductor is distributed when 20 A of current is put through the conductor. The medium surrounding the conductor is air.

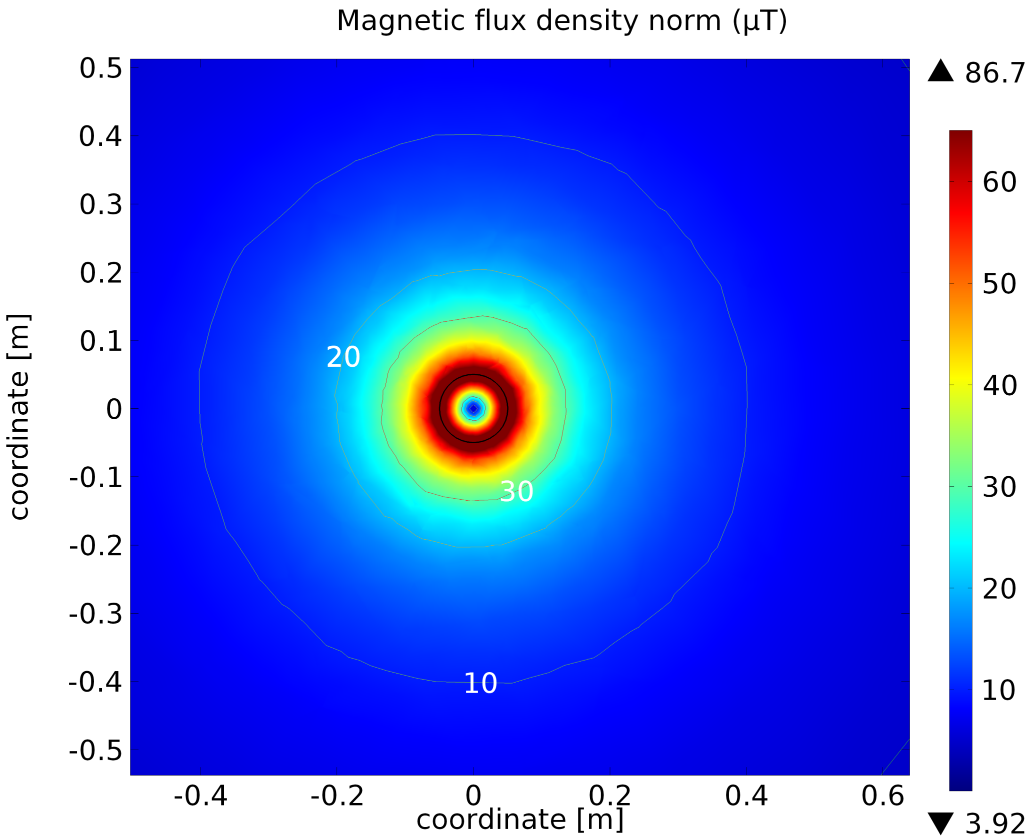

Figure 2.4: Finite element method (FEM) simulations of the ϕ-direction MFD surrounding single conductor with a 20 A DC running through it. Coordinates are in meters and the field is measured in μT .

2.1.2 Electric field

The electric field is described in Eq. 2.2 where q is the electrical charge and R the radius from the charge. ϵ is the permittivity, which can be described as the material constant that the measurement of $\mathbf{E}$ is performed in. This material dependency makes electric field measurements impossible when the environment properties are unknown.

$$\mathbf{E} = \frac{q}{4 \cdot \pi \cdot \epsilon \cdot R^2} \tag{2.2}$$

2.2 Power cable installation

Since the power cable infrastructure is a national matter the voltages in different phases of the transmission-chain differs. There are regional nets which distribute power transformed from the high-voltage transmission net, and in Sweden the voltage for these regional nets varies between 40-130 kV. To provide energy to customers connected to this regional net, the voltages are transformed down to a distribution net where voltages ranges from 10-20 kV [13]. The power cable detection equipment in this thesis should be able to detect both regional- and distribution net power cables.

2.2.1 Depths

The installation of underground cables is done at different depths depending on performance demands and overlying structures. In Sweden the minimum depth for cable installation is 0.45 m for cables below 22 kV and 0.65 m for cables rated 55-145 kV but power cables are buried at even greater depths [14]. The deeper a cable is buried, the lower the temperature in the surrounding soil. A low temperature allows a higher current. Therefore the deeper a cable is buried, the better the performance. An overlaying structure i.e. a road will place loads on a cable cable installation forcing it to be buried deeper than a cable without any overlaying structure [6].

2.2.2 Formation

There are two types of formation of power cables, flat or trefoil formation. In Figure 2.5 one can see both formations. The advantage with trefoil is that the conductors will cancel fractions of the electromagnetic fields generated due to the phase difference between the conductor currents. A flat formation will on the other hand make it easier to perform maintenance due to the separated distance of the cables.

Figure 2.5: Flat versus trefoil formation. The trefoil formation also comes as a single cable with insulation material in-between the conductors.

Simulation of cable formation and current in a lab environment requires properties regarding cable type, cable diameter and the inter conductor distance. The data for XLPE cables is in Table 2.1. XLPE cables are cross-linked polyethylene insulated cables [15]. The inter conductor distance is the distance between the middle of the conductor to the middle of the closest conductor(s). The main difference between the cable types is the inter conductor distances where 11 kV trefoil cables typically has $\approx$ 40 mm separation while the flat formation version has a $\approx$ 110 mm separation with a current rating of 500 A.

The 110 kV cables are a bit thicker and by looking at data from three different manufacturers in Table 2.2 it can be said that a typical inter conductor distance is 60-70 mm for a trefoil formation and 130-150 mm for flat formation.

Table 2.1: Single core power cable, aluminium conductor, XLPE insulated, 185 mm² cross area, 11 kV nominal voltage, ≈ 500 A current [5].

Company	Nexans	Nexans
Type	Trefoil	Flat
Outer diameter, D_e [mm]	39	39
Conductor diameter[mm]	16	16
Inter conductor distance [mm]	39	109

Table 2.2: Single core power cable, aluminium conductor, XLPE insulated, 400 mm² cross area, 110 kV nominal voltage, ≈ 500 A current [6, 7, 8].

Company	ABB	ABB	Prysmian	Prysmian	Nexans	Nexans
Type	Trefoil	Flat	Trefoil	Flat	Trefoil	Flat
Outer diameter, D_e [mm]	62	62	66	66	64.9	64.9
Conductor diameter [mm]	23	23	23	23	23	23
Inter conductor distance [mm]	62	132	66	150	64.9	134.9

2.2.3 Residual MFD

There are two main reasons for generation of uncancelled MFD surrounding a three phase system. The uncancelled MFD is often called residual MFD. The first reason for residual MFD is unbalanced loads. Unbalanced loads occur when the default load on each phase is not exactly the same. The loads are seldom completely balanced and the level of unbalance is individual for each power system and can not be foreseen. The second factor causing a residual MFD is inter conductor distance. Due to the phase difference of the phase currents any inter conductor distance $\neq 0$ will cause a residual MFD. In an ideal scenario(inter conductor distance=0) the emitted MFD would not exist due to cancellation.

The size of the residual caused by the inter conductor distance varies with a few parameters like formation, current, and the conductor separation. The conductor diameter can also be a factor if $D_{conductor} \approx$ Inter conductor distance since the current does not flow uniformly through a cable, the current rather travels closer to the surface of the conductor due to the electron polarity. In Figure 2.6 it can be seen how the MFD-norm fades with the distance from the conductor. In this figure the geometry is according to a 11 kV trefoil power cable and at 1 m from the cable center one can expect a MFD of a couple of μT .

In Figure 2.7(a) the MFD on a line 1 m above this trefoil 11 kV cable is plotted. A bell curve is observed since the distance to the center is at its lowest when measurement is performed straight above the center of the cable. The frequency of the power net is 50 Hz in large parts of the world and in Figure 2.7(b) one can see the MFD in a point right above the cable for one period. The negative part of a 50 Hz sinusoidal is "rectified" thus the signal becomes a 100Hz signal.

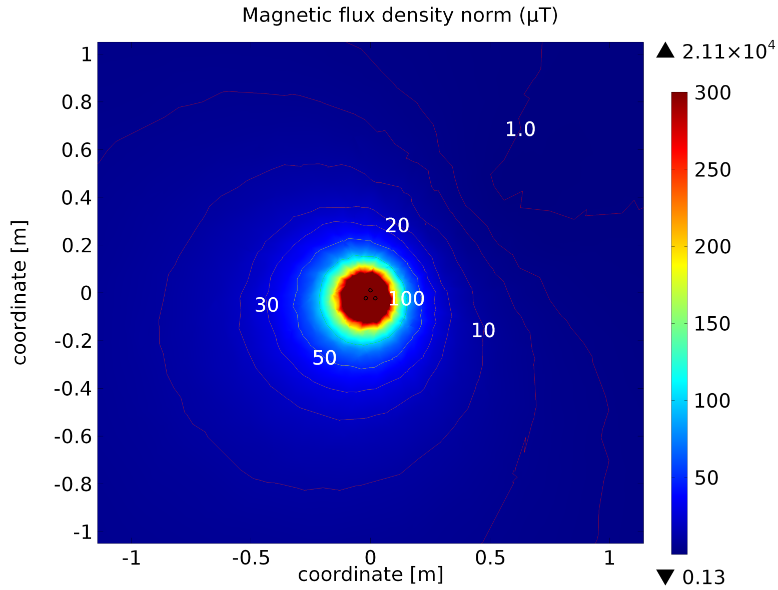

Figure 2.6: COMSOL simulation of MFD generated by a 10 m long 11 kV trefoil cable carrying 500 A per phase. Coordinates are in meters and the field is measured in μT .

In a flat formation power cable, as in Figure 2.8, the residual MFD is a bit higher due to the larger separation of the conductors. The separation causes the fluctuation to increase compared to that on a line above a trefoil cable. In Figure 2.9(a) the field peaks at 18 μT right above the cable. The point fluctuation for flat formation also fluctuates more than in the trefoil case as proved by Figure 2.9(b). The simulations show that the change in residual MFD is in the range of 1-20 μT .

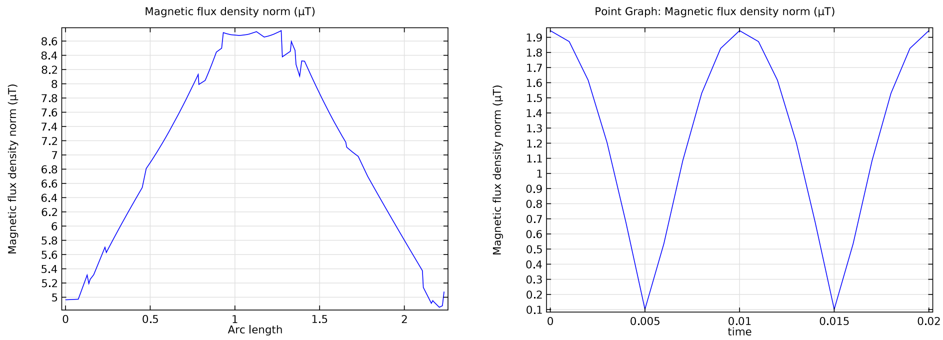

(a) Line MFD 1 m above cable. The middle of the x-axis is directly above the cable.

(b) Point MFD 1 m above cable at 0 to 20 ms.

Figure 2.7: COMSOL simulation of MFD on a line and for a point 1 m above cable center with 11 kV trefoil cable. 500 A phase current. Coordinates are in meters and the field is measured in μT .

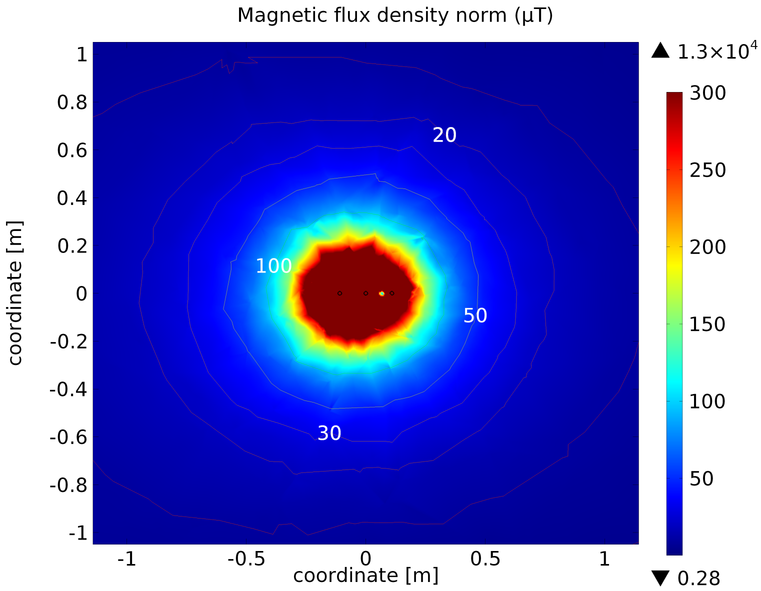

Figure 2.8: COMSOL simulation of MFD generated by a 10 m long 11 kV flat cable carrying 500 A per phase. Coordinates are in meters and the field is measured in μT .

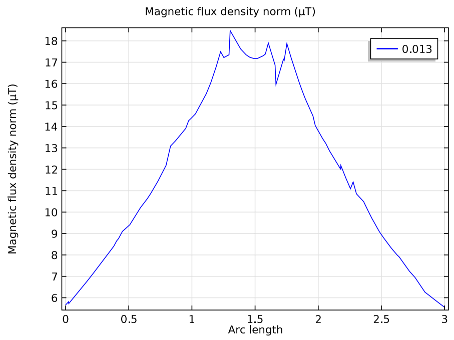

(a) Line MFD 1 m above cable. The middle of the x-axis is directly above the cable.

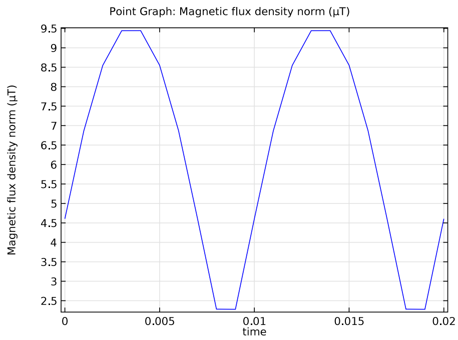

(b) Point MFD 1 m above cable at 0 to 20 ms.

Figure 2.9: COMSOL simulation of MFD on a line and for a point 1 m above cable center with 11 kV flat cable. 500 A phase current.

Accordingly with the theory in Eq. 2.1 the MFD on a 2x2 m land piece 1 m above an underground cable theoretically looks like in Figure 2.10 and Figure 2.11 with the cable running along the y-axis at x=0.

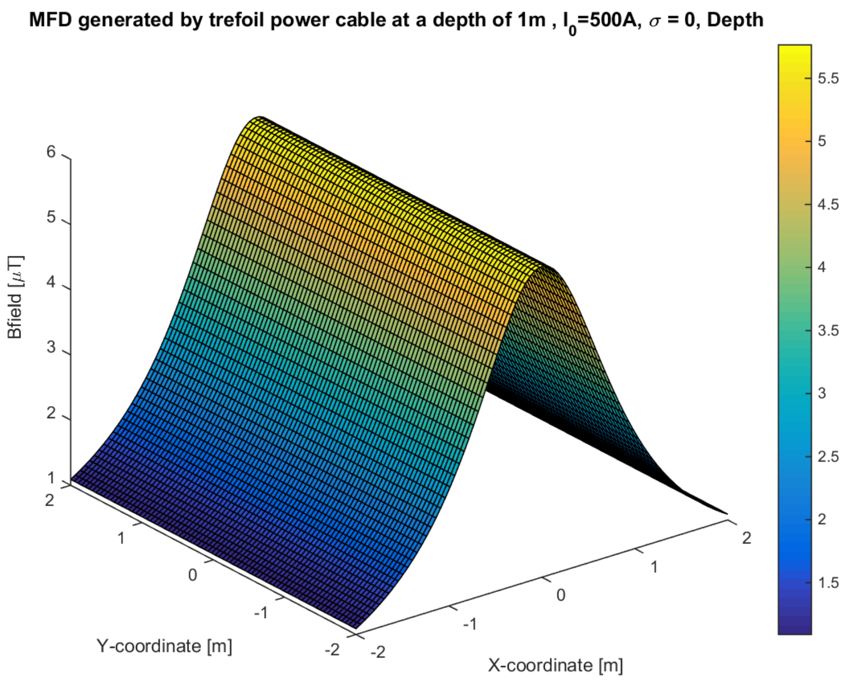

Figure 2.10: MATLAB simulation of MFD generated by a trefoil cable carrying 500 A per phase.

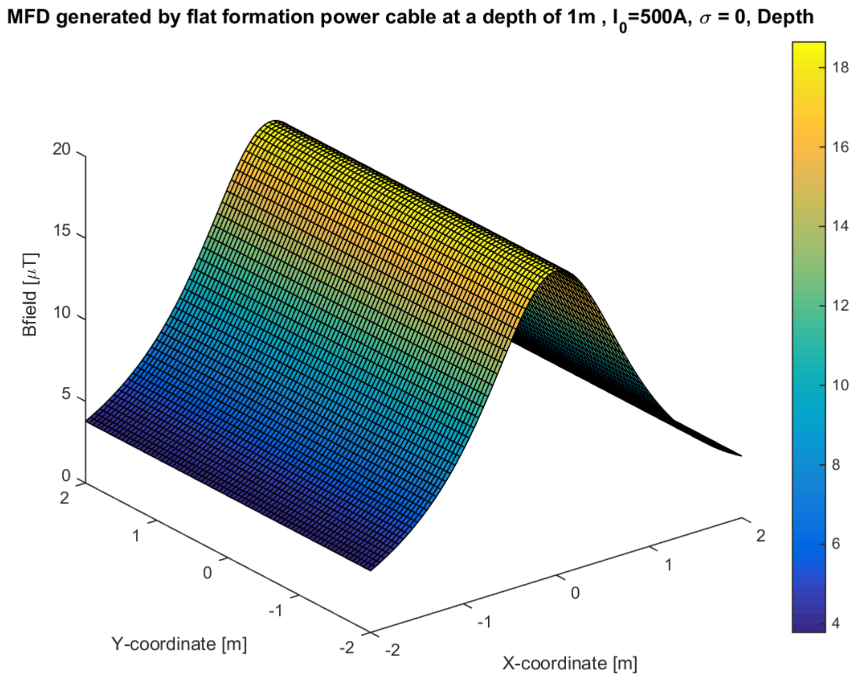

Figure 2.11: MATLAB simulation of MFD generated by a flat formation cable carrying 500 A per phase.

2.3 Magnetic sensing

Sensing magnetic fields is not a novel application. The compass is a magnetic sensor which points out the direction of the earth's magnetic field and it has been used for centuries for navigation purposes. Since invention of the compass magnetic field sensing has evolved to an industry that not only measures the earth's magnetic field but also other implementations such as brain activity, vehicle detection and fields generated by electric currents. Sensors which measure the magnetic field are called magnetometers. The theory of magnetometers in this thesis will focus on technologies that have a small feature size and can measure small magnetic fields. The sensor solutions are often expressed in a Microelectromechanical systems (MEMS) solution.

In today's market there is a multitude of different technologies available. The distinction between technologies are their measurement range and sensitivity. The MFD can have both Tesla [T] and Gauss [G] as unit for the MFD and the relation between Tesla and Gauss is given in Eq. 2.3.

$$1\ gauss = 10^{-4}\ T \tag{2.3}$$

The magnetic field entity is represented by a vector quantity that consists of magnitude and direction. The magnetic flux density is represented by the normal component of the magnetic field on a given surface. Simplified; the strength of the magnetic field. The variety of magnetometers focuses on different aspects of the quantity [2].

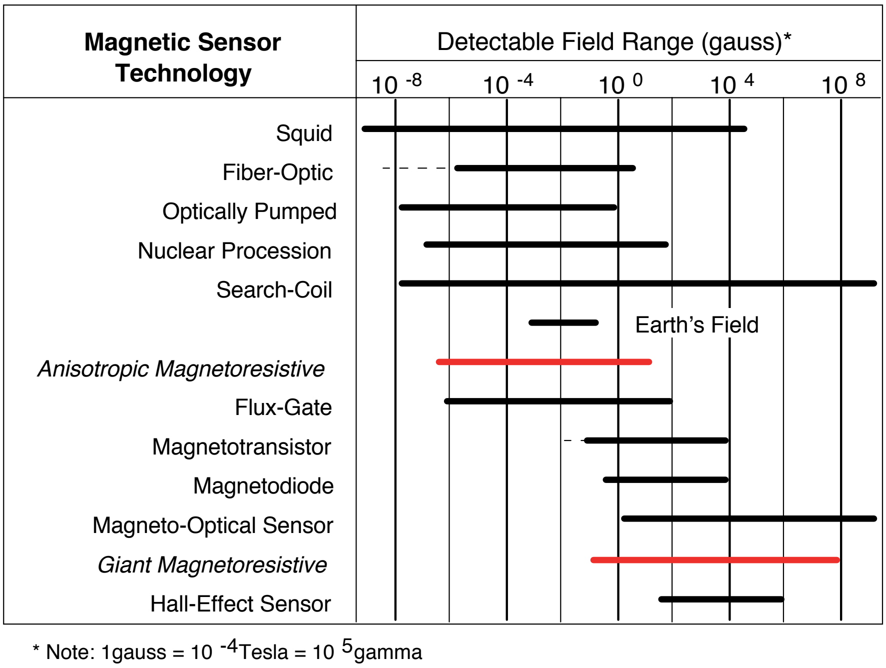

Figure 2.12: Magnetic sensor technology field ranges [2].

2.3.1 Magnetoresistive technology

Magnetoresistance is the change in a material's electrical resistance in response to an applied magnetic field [16]. This ferromagnetic effect is the fundamental behaviour observed in Anisotropic magnetoresistive (AMR)[1] sensors and Giant magnetoresistive (GMR) sensors. The ferromagnetic effect was discovered in 1856 by William Thomson [16]. AMR and GMR sensors are based on resistances with ferromagnetic abilities. These common magnetoresistve techniques offer a typical resolution of a few nT and measurement range from μT to mT [17]. The GMR technology offers a tenfold increase in sensitivity in relation to AMR [17]. There are several other magnitudes of magnetoresistive types under development. M. Ali *et al.* have presented a material which is described with a magnitude of extremely large magnetoresistive properties, which can be used for magnetic field sensing [18].

2.3.1.1 Anisotropic magnetoresistive sensors

The AMR effect is observed in materials that have the properties to change their electrical resistance when a magnetic field is applied from different angles [19]. This effect is based upon spin–orbit interaction, where magnetic fields cause shifts in the electron energy levels. The total energy level of the material is in turn changed due to the interaction between the spin of the electrons and the magnetic field. The change in energy level of the material leads to variations in conductivity, and thus the resistance of the material [20]. The AMR effect with respect to angle of the applied magnetic field can be seen in Figure 2.13.

[1] Sometimes called ordinary magnetoresistance (ODR)

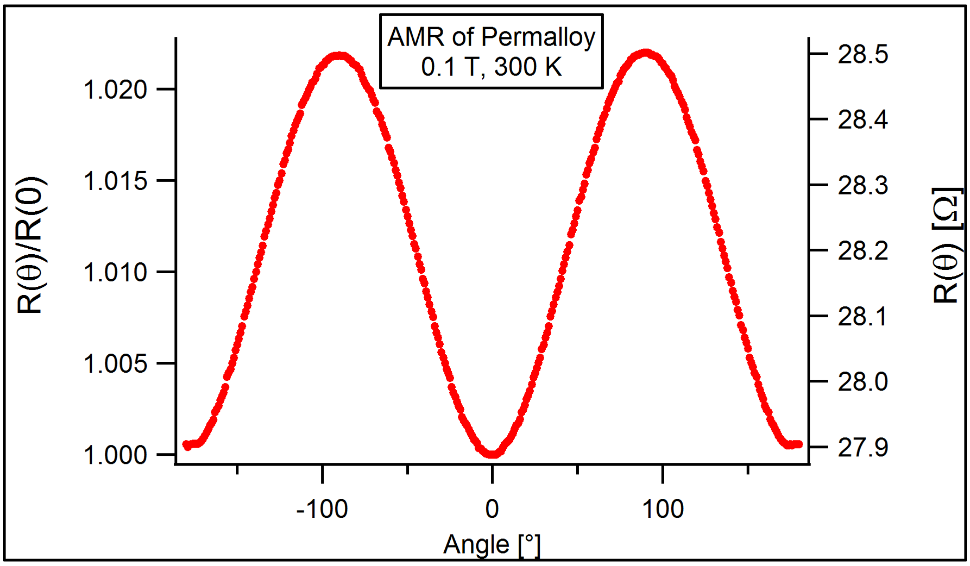

Figure 2.13: The AMR effect shown on a permalloy film [3].

AMR and GMR technology are commonly used in MEMS systems. A typical installation of AMR technology is to place the AMR resistors in a Wheatstone bridge to be able to measure the magnitude of magnetic field across its axis. Mounting three of AMR Wheatstone bridges in a orthogonal position position enables three dimensional measurement of magnetic fields. An example of a MEMS construction of AMR type is shown in Figure 2.14(a) and its transfer curve in shown in Figure 2.14(b).

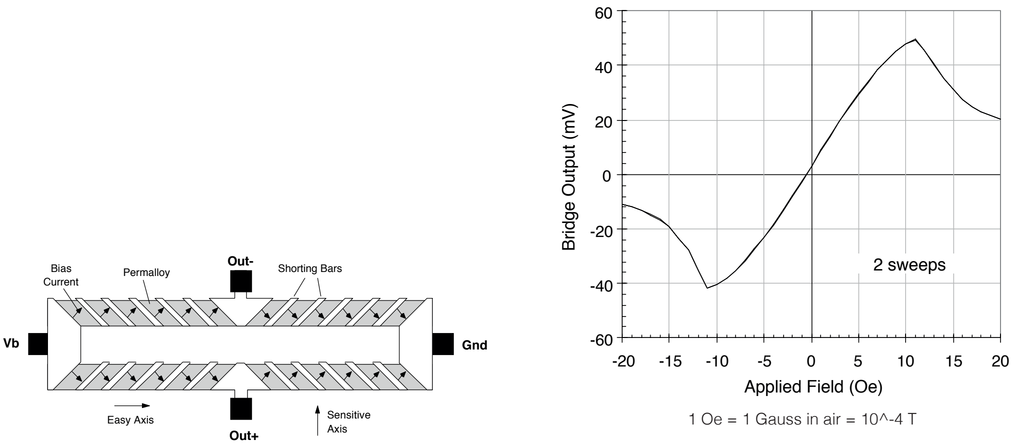

(a) Wheatstone construction of AMR type [2].

(b) AMR transfer curve [2].

Figure 2.14: Wheatstone setup (a) and bridge output (b) for AMR.

2.3.1.2 Giant magnetoresistive sensors

The GMR can observed by placing two thin layers of ferromagnetic materials placed on each side of a non-magnetic layer. When a magnetic field is applied the resistance of the ferromagnetic material changes and there is a larger resistance difference between the two ferromagnetic layer [21]. The effect occurs because of the inherit spin of the electrons in the lattice of a ferromagnetic material. As defined by the Pauli exclusion principle, electrons have different states, up or down. The resistance of the material changes drastically when changing between states[21]. The adjective *Giant* comes from its large increase in resistance when affected by a magnetic field.

Apart from the use in sensors the GMR technology is common in memory devices such as harddrives and RAM. GMR sensors are built as wheatstone bridges, just as AMR sensors. The difference between AMR and GMR is the materials used to form the resistance [22].

For the discovery of GMR Albert Fert and Peter Grünberg were awarded the Nobel prize in physics in 2007 [23, 24]. Today's GMR doesn't have equally good field range as the AMR, but research in this field is hopeful in finding new materials which improves both ranges and sensitivity [2, 22, 18]. Figure 2.12 shows a graphical overview of measurement range between AMR and GMR.

2.3.2 Hall effect sensors

Hall effect sensors are one of the most common technologies in magnetic sensing. Hall effect sensors are based on the Hall effect which utilizes the Lorentz force. The Lorentz force describes the force a charged particle experience from electromagnetic fields. The force can be used to measure the magnitude of the affecting field [25]. Hall effect sensors is a proven technique but seldom achieves the same sensitivity as the magnetoresistive technologies [26, 2]. Figure 2.15 shows the Hall effect, where the voltage fluctuations are measured to derive the magnetic field.

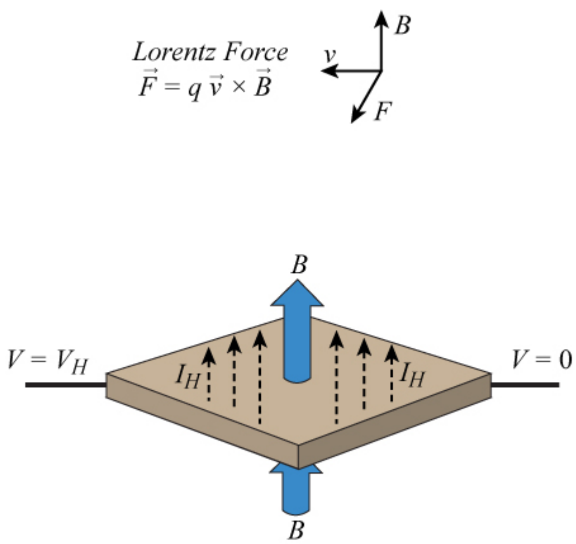

Figure 2.15: A schematic of the Hall effect [4].

2.3.3 Coil based magnetometers

This technology is often named search coil or inductive sensor. Coil based technology utilise Faraday's law of induction. As seen in Eq. 2.4 the voltage e is induced by the magnetic flux Φ and N is the number of turns of wire. Traditionally coil based magnetometers offer great sensitivity in the range of Hz to several MHz for larger coils [27, 2]. The technology has been proved in MEMS circuits but the technology is still in a research and not a production state [28].

$$e = -N\frac{d\Phi}{dt} \tag{2.4}$$

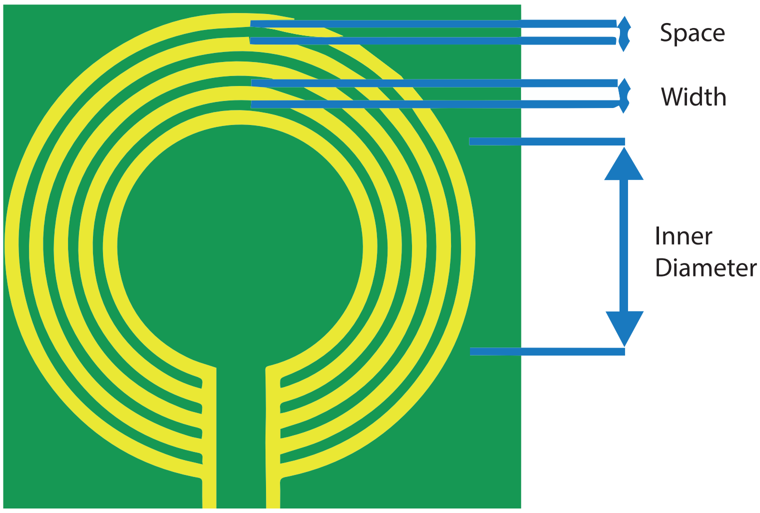

Figure 2.16: Design of micro-coil in a MEMS structure.

2.4 Inverse problems

While a typical problem is characterised by inputs to a function resulting in an end solution, an inverse problem is a problem where given a measured quantity one would like to find the input/cause of the measured quantity [29]. To be able to solve such a problem, a function describing the theoretics of the measured quantity together with an algorithm for input minimization is used. To exemplify, with the magnetic field function from Eq. 2.1 the inverse problem would be:

$$\min_{I_0} \quad |\mathbf{A}I_0 - \mathbf{B_{meas}}| \tag{2.5}$$

Where $\mathbf{A} = \mathbf{B}/I_0$ according to Eq. 2.1. If this equation is minimized the result is the I_0 which fits best to the vector of $\mathbf{B}_{meas}$ that is used as input [30]. By using an inverse problem formulation as in Eq. 2.5 together with continuous positioning optimization one can extract both the current and the position for the conductor.

2.5 Stochastic optimization and Artificial Immune Systems

According to Stochastic Optimization by Kirkpatrick & Schneider [31]:

> *"Optimization can be viewed as an exhaustive search, starting at some quite arbitrary place and then climbing or descending through a very rugged landscape searching for the highest mountaintop, or lowest valley (where altitude represents the quality of the current solution). "*
>
> *-J.J.Schneider & S.Kirkpatrich*

This quote describes the trade of optimization and how stochastic optimization can be used to solve some problems more efficient than conventional methods. Stochastic optimization is, as proposed in the quote, a method for solving maxima and minima problems in a very efficient way. By using stochastic variables in optimization the goal is to find the global maxima or minima for an objective function in a efficient way.

It is problematic when there are several mountains and valleys in the same search area. An example is presented in Figure 2.17. The algorithm may get stuck in a valley or on a mountain in the search for the extremes and it is hard to find the global extremes with traditional methods like Newton-Raphson when the landscape for analysis is complex.

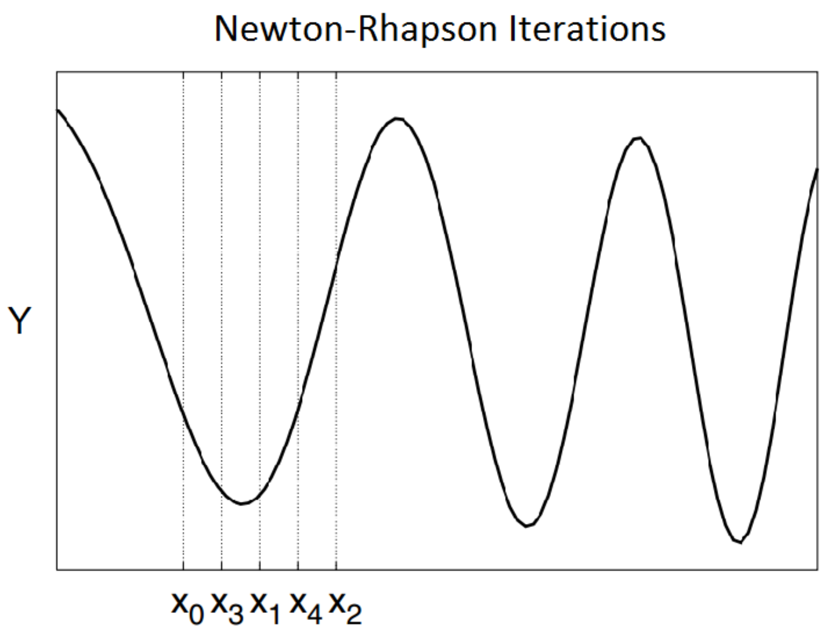

Figure 2.17: Newton-Raphson method for 5 iterations on an oscillating signal.

To solve problems using stochastic variables can radically decrease the calculation time for some types of problems compared to classic mathematical methods such as the Newton-Raphson method where each iteration cuts the search area in half no matter what. Another advantage with stochastic optimization is that there are algorithms that can detect several maxima/minima points at the same time, something that is hard to achieve by using the Newton-Raphson method in a case like that of Figure 2.17 without running the algorithm several times with controlled start/stop conditions [32].

Stochastic optimization can be applied in many different ways and on many different problems. Algorithms are developed continuously and stochastic optimization algorithms are constantly applied to new areas. Some types of problems where stochastical optimization is very relevant include classification of petroleum well drilling operations, defence against 802.11 DoS attacks and bankruptcy prediction, to mention only a few [33].

An interesting fact about stochastic optimization techniques is that the techniques often mimic biological systems e.g the genetics and immune system of the human body as well as the behavior of animals . The Genetic algorithm (GA) is an algorithm with a Darwinistic approach. Only the variables resulting in the most fit solutions of the iteration gets to reproduce. The reproduced variables are then stochastically spread around the parent variable. For the next iteration the space available for new offsprings will have converged and will continue to do so until the algorithm reaches either the point where error is lesser than the maximum error or the number of iterations are equal to the maximum number of iterations.

While GA is an interesting approach to stochastic optimization, it can only find one solution each run while the closely related algorithm Artifical immune system (AIS) can reach a condition with several solutions. The AIS algorithm is responsible for several steps in the collaboration with the object function evaluation [34].

1. Choose variables that creates most fit solutions for reproduction.
2. Reproduce in suitable constrained area around the fit variable.
3. Kill variables producing unfit solutions.

Just as other stochastic optimization algorithms and as the name may tell, AIS mimics the function of immune systems. The function of the immune system is to defend the body against the intrusion of bacteria and virus, hereby referred to as antigens. A simplified explanation of the immune system is as follows:

1. When the body is exposed to antigens, the immune system will produce antibodies.
2. Antibodies have an ability to find specific antigens and when the antigens are found the process of killing them begins.
3. The process of killing antigens stimulates the immune system to better recognize the same antigen next time it appears, and to faster recognize new antigens random mutations are introduced.

4. Similar antibodies are suppressed which enables a larger diversity of antibodies in the immune system.

When this function of the immune system is used in optimization, the antigens represent the optimal points of an objective function. The antibodies are the test configurations. By modifying the antibodies by mutation to fit the antigens as good as possible the algorithm can find the solutions. Since the antibodies can mutate to find to antigens the end result can be several solutions [34].

3
Hardware implementation details

Before the design of the detection algorithm was performed, tests to measure the MFD surrounding a power cable were conducted. According to the theory in Section 2.2.3 the detection application would need to be able to detect fields in μT size with a variation of $\approx 20\mu T$ if a sensor-to-conductor distance of 1 m is assumed. In Section 3.1 the sensor alternatives will be explained together with a motivation for the use of these technologies in the target application.

To extract the data from the sensor an acquisition system was built. The acquisition system was built around the sensor chosen as most fit and it needed to handle communication, presentation and sampling. The acquisition system is further explained in Section 3.1 and Section 3.2. A rig for testing the sensor together with the acquisition system and three conductors was constructed. The rig, hereby referred to as test rig, mimics the behavior of underground power cables and is further described in Section 3.3.

3.1 Sensor

There are several properties which are important for a magnetometer measuring the MFD generated by underground power cables. For this thesis future integration is also an issue and it is an advantage if the sensor solution can be integrated on an already existing inertial measurement platform.

3.1.1 Resolution

Since the residual MFD to be measured is of μT scale the sensor should be able to measure at least with 10x better resolution than this, and preferably with 100x better resolution to achieve reasonable Signal-to-Noise Ratio (SNR). The better the resolution of the sensor, the better precision of the detection algorithm spatial parameters.

3.1.2 Sampling frequency

In Figure 2.7(b) and Figure 2.9(b) one can see how the MFD in a point varies for a 50 Hz period. There are two events in each period resulting in a 100 Hz frequency for a 50 Hz power cable and 120 Hz for a 60 Hz cable. In order to be an eligible choice for sensor the Nyquist–Shannon sampling theorem has to be fulfilled resulting in a possible sampling frequency of at least 240 Hz. A higher sampling frequency leads to better SNR by applying methods such as oversampling [35].

3.1.3 Integration

For the design to be an eligible option for integration with already existing electronics and not just for test, the components for the hardware implementation were chosen with parameters like size and interface in mind. A small size allows for a more flexible placement on an excavator while the interface must be compliant with the data acquisition system. The design should enable performance that allows as high as possible sampling rate.

3.1.4 Sensor analysis

As explained in Section 2.3 there are many different types of sensors and while some are not relevant for this project based on their detectable field range, some are excluded due to not enough market alternatives and unreasonable cost. The sensors in the range of 0.1-20 μT , as derived in Section 2.2.3, are in most cases AMR sensors due to availability and size.

GMR technology seemed like a reasonable competitor in theory, but unfortunately the research and commercialisation has not come as far for GMR as it has for AMR technology. The options that exists are either very expensive or not in production by the time this thesis was written.

In Table A.1 relevant sensor properties are presented. Some of the sensors were excluded because of their low sampling rate. Since many magnetometer Integrated circuit (IC)'s are compass function purposed, the sampling-rate is not high enough to meet the demands on a system for power cable detection. The only sensor with a digital interface which meets the sampling frequency demand is the Freescale FXMS3110. The sensor has a low noise rating (0.3 μT) but after tests it was discovered that this noise level was only achievable if using the lowest sampling rate available while the noise at the maximum speed was $\approx$ 1.2 μT . The SNR of the output could not be accepted.

Other suitable sensors are the analog Honeywell sensor types HMC1053 and HMC2003. The HMC2003 comes with a few more integrated functions than HMC1053, such as amplifiers, internal reference and top of the line resolution. The HMC2003 is more expensive and larger in size than the HMC1053 which is the reason for choosing HMC1053 for the hardware system. The fact that HMC1053 comes with less extra functions allows the PCB design to be smaller and more tailored to the specific needs of the application.

3.1.4.1 HMC1053

The HMC1053 comes in several packaging options but the most fit for a PCB is the 16-pin LCC Quad Flat No-leads package due to its compact dimensions. In Table

3.1 the most relevant information from the HMC1053 datasheet is presented. The supply voltage can be set to a large range of levels. A lower supply voltage would lead to a lower bridge output voltage, which has to be matched with amplification parameters. The supply voltage has to be chosen with system components such as amplifiers and Analog-to-Digital converter (ADC)'s in mind to meet both resolution and range demands.

The bridge resistance is important in the sense that it together with the supply voltage sets the current through the component. A 5 V supply system means 12 mA (three bridges in parallell) while a 20 V system would give four times the current. Since the bridge current will probably account for most of the PCB current consumption the current to the bridge must be kept low. By keeping the supply current low to the bridge this enables the unit to be supplied by the sensor network's power source or maybe even a battery.

To get as good measurements as possible the sensor supply voltage needs to be low-noise, preferably from a Low Drop-Out (LDO) regulator and not a switching converter. The LDO regulator is linear and has no switching noise compared a switching buck converter but it burns of the overvoltage as heat, thus increasing energy consumption. A buck converter in series with a LDO is the best solution to a good quality supply voltage whilst the power consumption is kept low.

Since the sensor is to be placed in a harsh environment, the operating temperature has an importance. A -40 to 125 C° range is suitable for most environments and the sensor is in Honeywells Defence & Aerospace component product range. A 0.1 % linearity error within a $\pm 100\mu T$ range is acceptable for this project since the expectations is a magnetic field fluctuation of 20 μT . Even though the MFD fluctuation is expected to be small, there will always be a small offset created by the earth's magnetism and other effects such as hard iron and soft iron effects which demands us to use a Gauss sized working range.

Table 3.1: A table with important information extracted from the HMC1053 datasheet [9].

Characteristics	**Min**	**Typ**	**Max**	**Unit**	**Conditions**
Supply	1.8	3	20	V	
Bridge Resistance	800	1000	1500	Ω	
Operating Temperature	-40		125	C°	Ambient
Linearity Error		0.1		% FS	$\pm 100\mu T$ range
Sensitivity	0.8	1	1.2	$\frac{mV}{V_{100}\mu T}$	
Set/Reset Strap Resistance	3	4.5	6	Ω	
Set/Reset Strap Current	0.4	0.5	4	A	0.1% duty cycle, or less, 2 sec current pulse

The sensitivity rating describes the sensor output under given working conditions. For a situation with $V_{DD} = 4.5V$ and a smallest detectable field of 0.1 μT the sensitivity will be:

$$V_{sens} = 10^{-3} \cdot V_{DD} \cdot 10^{-3} \left[\frac{V}{0.1 \mu T} \right] \tag{3.1}$$
$$= 4.5 \left[\frac{\mu V}{0.1 \mu T} \right] \tag{3.2}$$

The output for field changes of 0.1 μT will lead to a voltage change of 4.5 μV which is a quite sensitive resolution. To achieve this sensitivity it is stated that a set/reset has to be done before collecting a series of measurement and especially after having the sensor exposed to strong fields. A strong field could be generated by the metal body of an excavator for example. The set/reset strap is shown in Figure 3.1. The set/reset strap will create a current through the AMR resistor permalloy to realign its permalloy structure which improves and restores the sensitivity of the sensor. Since the set/reset analog electronics current loading/control circuit is built with capacitors it will not consume more than μA currents on average and therefore there is no needed for over dimensioning of the Power supply unit (PSU). The set/reset circuitry is not integrated in the magnetometer package but has to be constructed on the PCB with an Microcontroller unit (MCU) controlling it [9].

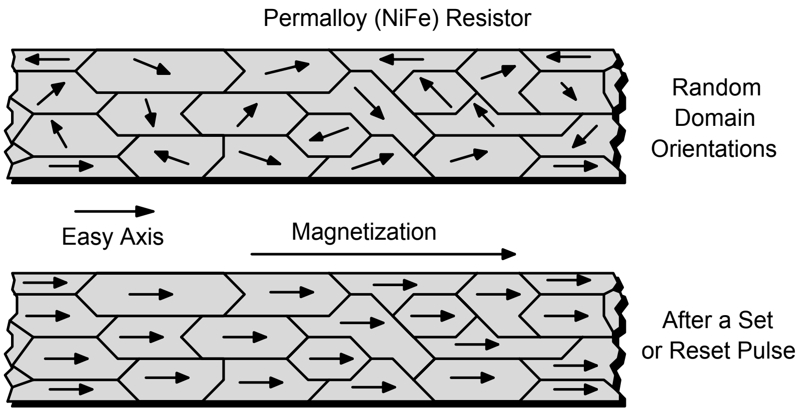

Figure 3.1: A set/reset pulse shown on a permalloy film [2].

3.2 Acquisition system

In the block diagram in Figure 3.2 the acquisition system is represented as five major blocks. This representation can differ depending on what components are used. Some sensors include amplifiers, some MCUs include ADCs etc. To handle communication, presentation and sampling each component of the acquisition system is important.

To be able to capture the bridge voltages from the sensor at the voltage stated in Eq. 3.1 the choice is between using a high precision ADC with a sub μT noise voltage reference, or to use an amplifier and then an ADC with a bit lower performance demands. Since the bridge voltage is very low for desired magnetic field sensitivity the reference noise would have to be below this to produce results.

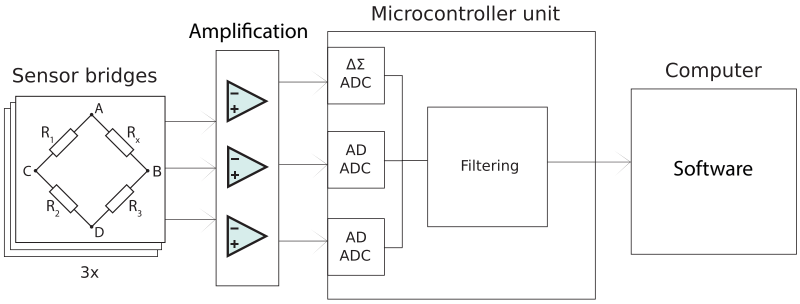

Figure 3.2: A system overview of the signal processing chain of the proposed aquisition system design.

The instrumental amplifier of choice will be described further in Section 3.2.1 while Section 3.2.2 will introduce the microcontroller.

3.2.1 Instrumental amplifier

Parameters as gain, reference and supply voltage for the instrumental amplifiers depend on the ADC. All ADC's has an Effective number of bits (ENOB) which sets the effective number of bits of the converted digital signal. To start with, the gain is calculated to have the largest desired output from the magnetometer, then mapped to the largest value that the ADC can capture. By doing the most noisy bits of the ADC can be overlooked. The factors which limit the range of the ADC is the available supply voltages and since the most stable PSU-voltage available in the hardware will be 4.5 V, this is chosen as supply voltage for the ADC analog supply as well as the instrumental amplifier supply voltage.

The HMC1053 has a range of ± 600 μT but a larger range also leads to less resolution. A limiting factor which can create an offset in the measurements is the earth's magnetic field which reaches ≈100 μT momentarily and to take some height for disturbing single conductor cables etc, a range of ± 200 μT is chosen. This range leads to a maximum output of ± 200 V_{sens} = ± 9 mV in both directions around the amplifier reference point. If this top-value is to be amplified to match the maximum output range of the amplifier and the reference-point is biased in the middle of this span, the desired amplification is:

$$G = \frac{2.25}{0.09} = 250 \tag{3.3}$$

The demand for an instrumental amplifier in a signal chain amplifying the bridge-voltage of HMC1053 and suppressing the common voltages is to be able to amplify 250 times at frequencies of $<$ 1 kHz. The amplifier must have a reference level input and be able to run at 4.5 V supply-voltage. An instrumental amplifier with a high Common-mode rejection ratio (CMRR) as possible is desirable. To meet these requirements the Texas Instruments INA129 is used. INA129 is a 1-channel, 3-OP in-amp, low power, precision instrumental amplifier which meets the above stated requirements [36].

3.2.2 Microcontroller unit and ADC

The choice of MCU, is decided upon key features such as interfaces and processing power. The end product should be able to perform analog-to-digital conversions and interface with other units by CAN and Universal asynchronous receiver/transmitter (UART). ST Microelectronics offers a suite of integrated circuits that are built upon ARM architecture. The ARM architecture relies on a well proven concept and with ST Microelectronics several product families a suitable MCU could be found [37].

The choice for MCU was the STM32F373 microcontroller together with an instrumental amplifier to amplify the signal produced by the bridge. This model includes an integrated 16-bit sigma-delta ADC - removing the need for inter-circuit protocols such as I^2C or SPI. Some high performance standalone ADCs like the ADS1258[38] was evaluated but two setbacks of using a standalone ADC is its larger size and that it will need to send the data to the MCU which limits the maximum achievable sampling rate. This led to the design choice of a MCU with an integrated ADC.

The STM32F373 includes three on-board sigma-delta 16-bit ADCs allowing sampling of the three magnetometer output channels without having to multiplex the signal. In addition to its existing interfaces and converters the circuit also offers digital signal processing blocks that could be used for filtering and processing of converted data. To calculate the noise properties and resolution of this system considering ENOB, some calculations needs to be conducted. Considering the ENOB:

$$ENOB = \frac{SINAD - 1.78}{6.02} \tag{3.4}$$

With a Signal-to-noise and distortion ratio (SINAD) from the STM32F373 datasheet at $\approx$ 76 dB ENOB would be 12.32 bits [37]. If the 4 Least Significant Bit (LSB) is avoided, the voltage corresponding to the 5th bit is valued 1.104 mV. To get this value in MFD:

$$B_{5thbit} = \frac{V_{5thbit}}{G * V_{sens}} = \frac{1104}{225 \times 45} = 0.109\mu T \tag{3.5}$$

A MFD of 0.109 μT for the LSB noise-free bit meets our minimum requirement for resolution.

3.2.3 Power supply unit

The specifications on the PSU are that it will have the ability to feed of CAN-network voltages from of an excavator. The PSU outputs will be regulated down to into three different supply voltages, 3.3 V, 4.5 V and 5 V for the boards different components. The 3.3 V signal is for the logical signals, the 5 V for peripherals demanding a higher supply voltage and the 4.5 V supply is a low noise analog electronics supply voltage.

The specifications are achieved by using DC-DC step down converter, which is rated for 65 V input voltage, to lower the input voltage to 5 V. This 5 V voltage supplies two LDOs converting the 5 V's down to 3.3 and 4.5 V. The PSU is also designed to handle transients, surge currents and coupled noise that can occur in a automotive environment.

3.2.4 Interfaces

To be able to send/receive data to other units such as inertial measurement sensors, Electric control unit (ECU)'s and PC communication interfaces was integrated with the design.

3.2.4.1 CAN

In vehicles the message standard for ECU communication protocol is CAN. To integrate the cable detection module in this environment a CAN bus interface is made available on the board.

3.2.4.2 UART

The UART protocol is implemented in the cable detection module to allow quick debugging via serial interfaces to a computer.

3.3 Test rig

In order perform accurate repeatable measurements to verify the relation between simulations and the sensor in hardware a good test rig is important. To verify and test the custom PCB built for MFD measuring purposes a test rig in two main parts was build.

Since no installed cables could be tested and a high enough current was not available some compromises were needed. Based on the theory in Section 2.2 the tests were performed with the maximum current from a 16 A standard fused power connector. The load was a 9 kW industrial heating fan. Since the maximum possible current was limited, this was compensated using longer inter-conductor distance than in the cables presented in Section 2.2. In the trefoil formation an inter-conductor distance of 100 mm was used instead of a ≈65 mm distance in real cables. In flat formation a separation of 150 mm was used which is the longest separation found on the market.

In Figure 3.3(a) and Figure 3.3(b) the different formations can be seen together with the rest of the setup. The test rig consists of one unit to emulate the underground power cable geometries and the other unit is a mount with five fixed positions for emulating the sensor sweeping over the underground power cable. The mount is placed on two tripods and thereby enabling an adjustable height setting for the Cable Detection Unit (CDU). The bottom panel is connected to the industrial heating fan acting as a resistive load. The setup is connected via a three-phase cable connector. With the fan turned on, the phase current is 13 A (RMS) measured with a clamp-amperemeter.

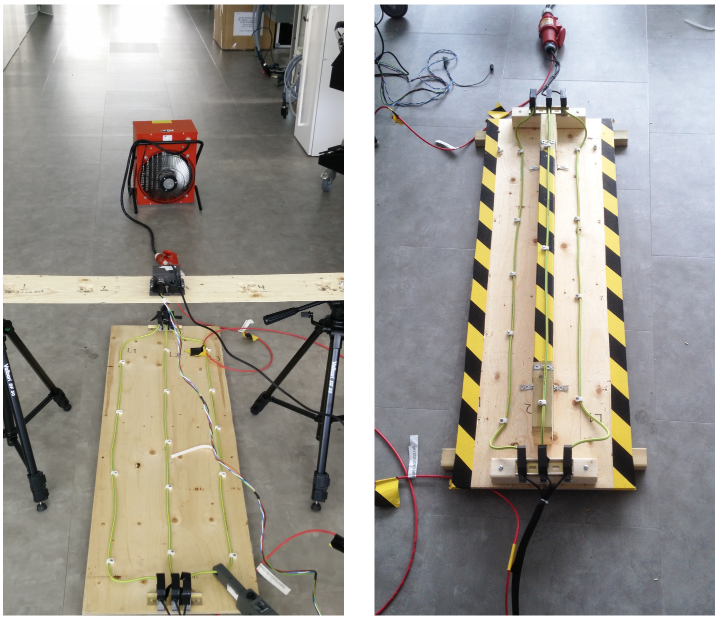

(a) Test rig for flat formation (b) Test rig for trefoil formation

Figure 3.3: Different variations of the test rig setup

The sensor itself is mounted in a metal casing to make it easier to mount. The casing in Figure 3.4 is also the suggested casing for later mounting the CDU on an excavator arm. To the left is the CAN connector acting power supply, then a grey programming cable and rightmost an UART cable transmitting the sampled data to a computer.

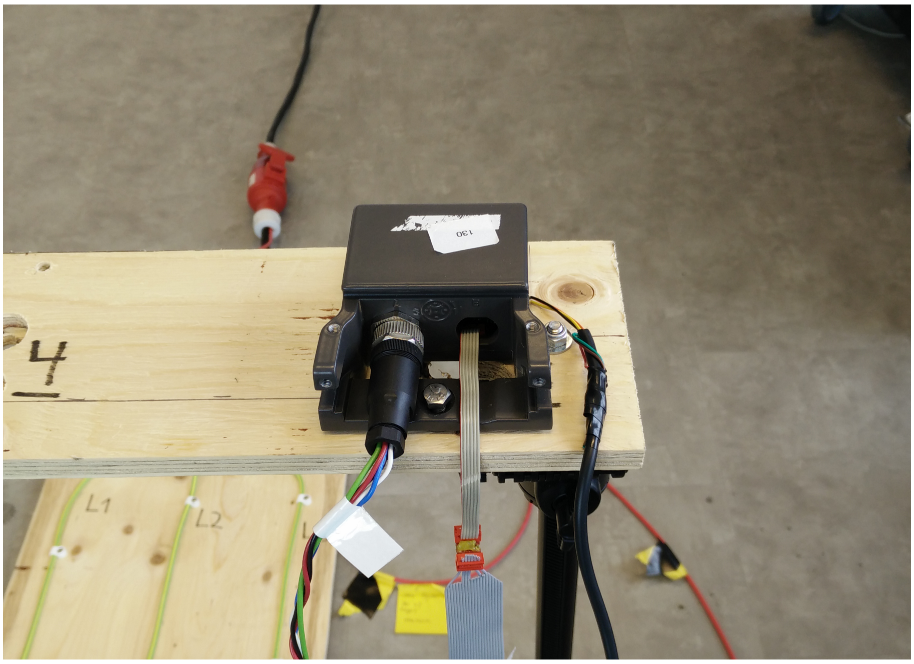

Figure 3.4: The cable detection unit mounted above the conductors.

4

Software implementation details

The software described in this chapter is not hardware oriented code like MCU-software but software for the post-processing methods suggested for the system. These post processing methods are to be tested on a PC and then the methods will be considered for integration on the MCU in a later stage.

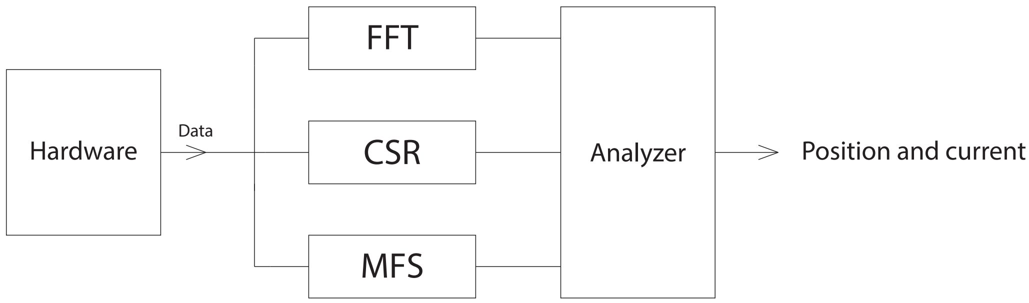

Figure 4.1: A software system overview. Illustrating the different computing blocks of the system.

There are several interesting methods for detecting underground power cables. In Figure 4.1 an overview is presented. At first the hardware provides data as described in Section 3.2. Then three methods for evaluating the data are used. In this thesis, the three methods will be evaluated standalone and suggestions for how to combine the methods will be suggested. The three methods are Fast fourier transform (FFT), CSR and Mean field strength (MFS). These post processing methods will then be combined in the analyzer to output information about the environment that have been measured.

In Section 4.1 a proposed detection algorithm based on frequency analysis will be presented. In Section 4.2 a CSR algorithm using inverse problem theory from Section 2.4 together with stochastic optimization and artificial immune systems from Section 2.5 in combination is described. The MFS will look at the overall strength of the oscillation at a position and is further descibed in Section 4.3.

For some of these methods a cross section view of the cable is needed, and to achieve this from our 3D measurements a mapping method is needed. This is described in Section 4.4.

4.1 FFT

In Figure 2.7(b) and Figure 2.9(b) a prominent 100 Hz signal is present. The expected signal content for an FFT of the MFD is a small 50 Hz component and 100 Hz with its harmonics. By looking at the signal spectrum of data collected in an environment where a power cable is present and comparing it to data collected in a zero-current environment it can be decided if a current conducting power cable is present.

As concluded in Section 3.2.2 the noise floor of the hardware system considering ENOB is $\approx 0.1\mu T$, therefore the SNR will be low if μT -size fields are expected. Even though the SNR can be quite low at the lowest currents, it is still expected to be distinguishable from a zero current environment.

4.2 Current source reconstruction

A CSR algorithm will from 2D (Depth/width) **B** -field measurement data combine inverse problem together with stochastic optimization theory in the form of AIS and output a cable centroid position as well as a current. Inverse Problem and AIS is further explained in Section 2.5 and Section 2.4. To create the 2D data from 3D measurements the mapping method from Section 4.4 is used. The algorithm has a few blocks as presented in Figure 4.2 where the first three blocks handles the initiation phase while the last 4 steps is a loop limited by exit and end conditions.

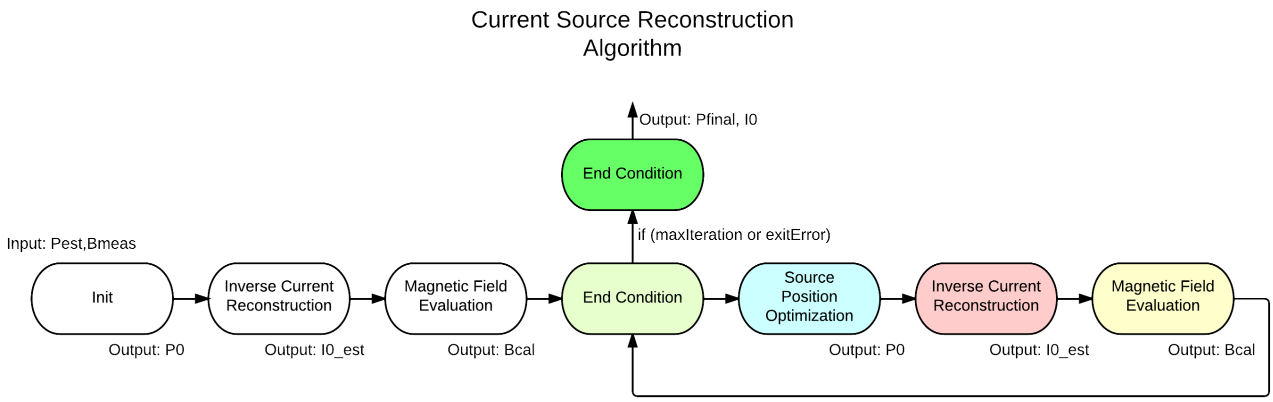

Figure 4.2: An algorithm mixing the concept of inverse problems from Section 2.4 and stochastic optimization and artificial immune systems from Section 2.5.

The blocks in the initiation phase are:

1. **Init**
   This block will with the estimated position and other measurement space parameters create a starting setup of coordinate guesses for the conductor centroid in a predefined area.

2. **Inverse Current Reconstruction**
   With coordinate guesses as input the inverse current reconstruction block will fit an object function describing the MFD with an optimal I_0 estimation for all P_0 as output.

3. **Magnetic Field Evaluation**
   The magnetic field evaluation will use the coordinates P_0 and the current estimations $I_{0,est}$ to calculate the magnetic field with the same object function as in the inverse current reconstruction. The output is B_{cal}.

These three blocks lead to a loop. The loop end condition is the `maxIterations` while the exit condition is the `exitError` which will end the loop when the error for the best match has gone below the exit error. The blocks in the loop are:

1. **Source Position Optimization**
   The source position optimization block will get the most fit values of P_0 and create a new P_0 from them. The spread of the new coordinate-space is dependent on the quote of the current error divided with the last iteration error to make the stochastic variable adaptive.

2. **Inverse Current Reconstruction**
   Same function as in the initiation phase.

3. **Magnetic Field Evaluation**
   Same function as in the initiation phase.

When the loop meets either the end or the exit condition the output is the P_0 coupled with the smallest error together with the reconstructed current for this.

4.3 Mean Field Strength

The quantity MFS is calculated through a simple formula measuring the amplitude of the oscillation of the measurements. For each direction the mean is calculated and subtracted from the signal to get just the oscillation. The resultants of the two vectors is calculated according to Eq. 4.1.

$$B_{res,i} = \sqrt{B_{x,i}^2 + B_{y,i}^2} \tag{4.1}$$

When the resultant is calculated the Root mean square (RMS) value for the signal is calculated as a measure of the field strength in one number.

4.4 3D - 2D mapping

Measurements from the sensor placed on an excavator arm will be subject to both vibrations and rotation. The measurements will not be on a straight line but on an arc due to the rotation of the excavator. To simplify and make calculations possible the 3D-measurements are mapped to a straight line in the cross section plane of the cable. To place the plane as a cross section of the conductors three things need to be calculated:

1. Point with largest magnetic field.
2. Strongest direction of the magnetic field (which is perpendicular to the conductors)
3. New transformed positions placing measurements on a 2D XY-axis plane.

In Figure 4.3 an arc representing the movement of the sensor on an excavator arm has measurements M1-M7. The excavator rotational centre is marked and an axis showing the direction in which the operator wants to measure is indicated. The figure is in a top perspective of the ground while XY is a ground plane, Y is a depth plane. In the example M6 is above the conductors and will measure the strongest magnetic field.

To decide the strongest direction of the magnetic field, time series measurements in all points are analyzed. The impact of the directions derived from measurements can be weighted, in such a manner that the points closer to the strongest field point are more worth than more distant measurements which are more probable to have a low SNR.

When the largest direction is calculated one can create the XY plane intersecting with the point with the strongest field, in this case M6. Since the field is distance-from-conductor dependent the points are transformed to this new XY plane, causing them all to be on one single line in the XZ plane. In Figure 4.4(a) the transform of the points to the XY-plane is shown.

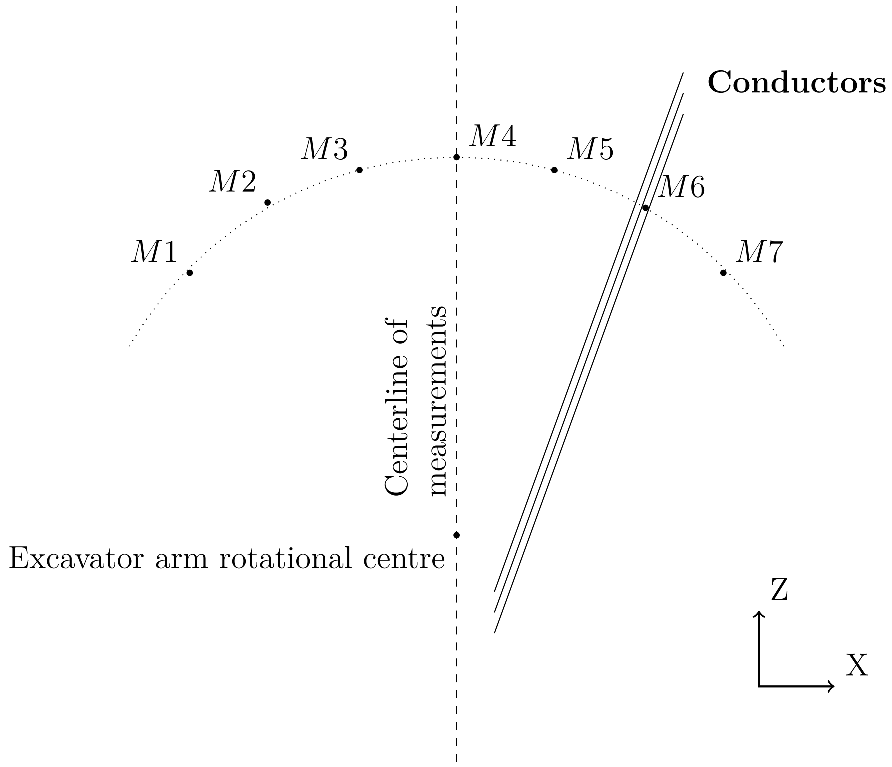

Figure 4.3: A top view showing measurements taken from an excavator arm mounted CDU.

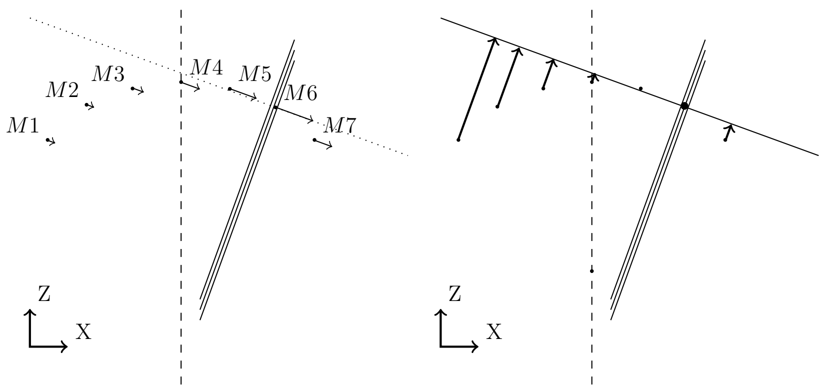

(a) The magnetic field in M1-M7.

(b) The transformation of M1-M7 to the new found cross section line.

Figure 4.4: Illustrations of the direction-calculation as well as the transformation.

5
Results

The results in this chapter consist of simulation based results, prototype development and algorithm performance. The simulation results regarding the MFD surrounding conductors, the FFT of the theoretical MFD and the AIS-algorithm run on data created by the theoretical models are presented in this chapter. The model data that is the basis for these measurements is generated using the same settings as when data was captured by the test rig. These results provide a base to compare with to see how the theoretical aspect of the problem differs from the real world data. These results will be presented in Section 5.1. In Section 5.3 the custom PCB which has been created to support the sensor and its functions are presented. The analysed measurements are presented in Section 5.4. The data collected from series of measurements in different positions and on different heights above the cable centroids are analysed by calculating mean MFD, FFT and inputting the data into the AIS-algorithm.

5.1 Simulations

The goal of the simulations was to find the MFD for the proposed test rig. The simulations performed laid the foundation of the specifications used in the design of the printed circuit board. Since a real power cable could not be tested the MFD of the test rig acts as a minimum demand for the system's ability to be able to detect power cables. A higher MFD is expected when measuring the field from real power cables. As seen in Figure A.1 an estimate of 1.0 μT was expected at 0.8 m.

By sweeping from left to right above the cable, a line of measurements is produced. These simulated measurements in Figure 5.2(a) show how the MFD increase as the point of measurement moves closer to the conductor centroid. Information about frequency content and amplitude is collected from the simulation in Figure 5.2(b). The time variation of the field in point measurement is on display in this plot where the frequency of the signal MFD is 100 Hz and the field oscillation is at $\approx 2\mu T$.

5.1.1 Detection simulations

By using data generated from cable models the SNR of the signal at positions above the cable is calculated. In Figure 5.3 and Appendix. A.2 the SNR value counting the 100 Hz component as signal energy is plotted. The flat formation produces a more sharp curve for the SNR than the trefoil formation whose curve is wider but with

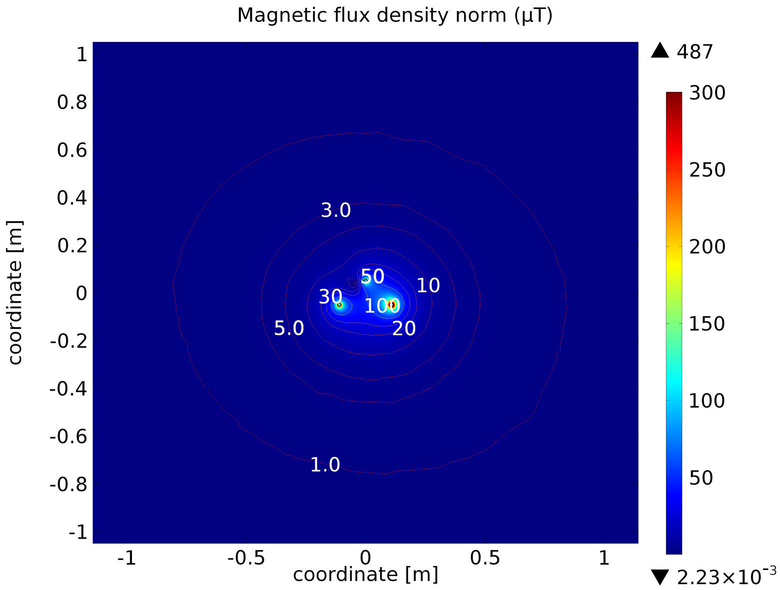

Figure 5.1: COMSOL simulation of MFD generated by a 1.5 m long trefoil formation cable carrying 13 (RMS) A per phase.

roughly the same span between high and low SNR-values. The difference between the peak values and the "floor"-level in the graph is not a very big one and may not be as distinguishable when the FFT is later calculated with the measurements. No noise have been added to the simulation data and therefor the SNR-level will not be entirely comparable between calculations made with simulation data and measured data.

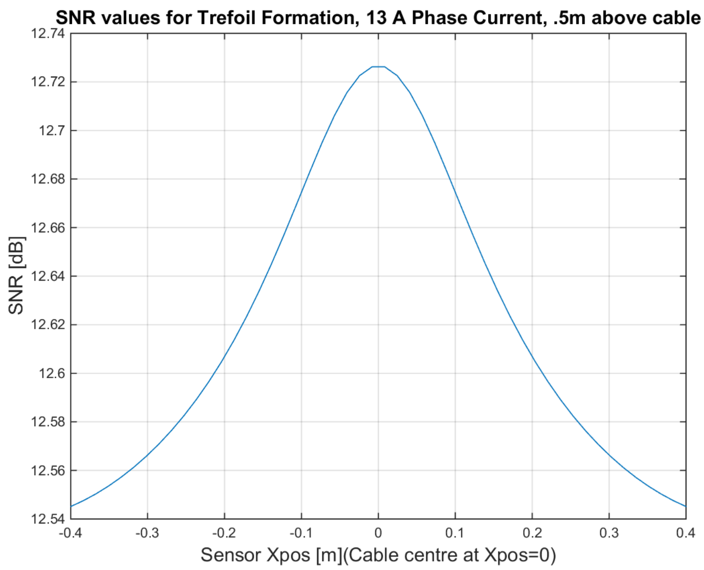

Figure 5.3: The FFT of a trefoil formation cable with 13 A (RMS) phase current, measured at 0.5 m above the centroid.

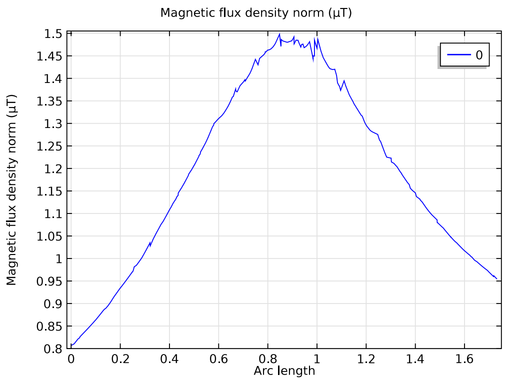

(a) Line MFD 0.5 m above cable. The middle of the x-axis(Arc Length = .9m) is directly above the cable.

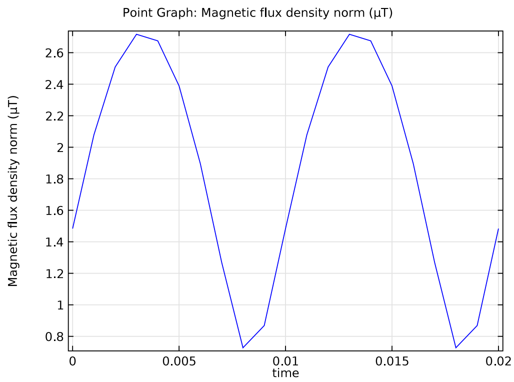

(b) Point MFD 0.5 m above cable at 0 to 20 ms.

Figure 5.2: COMSOL simulation of the MFD viewed in a line and point measurement. Height of the simulated measurement is 0.5 m, with conductors carrying 20 A per phase.

5.1.2 Current Source Reconstruction

In Figure 5.4 one can see the CSR-algorithm in action. Simulated data for a 500A trefoil cable is used as input. The conductor is simulated to be placed at (0,-1). The first guess of solutions is randomized and as the algorithm advances, the solution-space converges. The example in the figure is run to a maximum of 5 iterations and one can clearly see how the solution space shrinks for each iteration.

The number of measurements for this case is 5 and this example shows that this number of measurements is enough for finding the cable position. The mean position of the last sample space is marked in the close up with a black cross. The red ring surrounding the cross is the standard deviation of the last iteration. The conductor position using this method is found with a centimeter error.

5.2 Software

The functions now run on a PC is profiled to aid decisions regarding putting calculations closer to hardware. In Table 5.1 the profiling results for the CSR is presented. The most time consuming function is the MFD generation in BfieldGen, a function called in BfieldGen and the residual field calculated in Bfield3Phase.

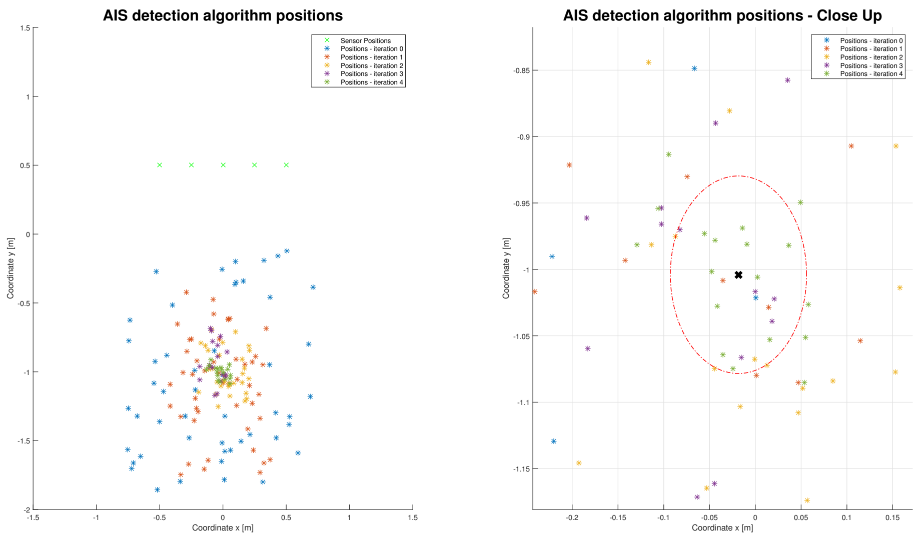

Figure 5.4: Results from the detection algorithm fed with simulated measurement data. The left plot shows the sensors positions and the iterations of the algorithm. The right plot shows a close up around of the last iteration. X/Y-axis are in meters [m].

Table 5.1: Profiling results from running the AIS-script in matlab. The program was run on an Intel Core i5-3317UM processor. The top 6 time consuming functions are sorted after self-time. The self time is the time the function have been in it self excluding child functions.

Function	**Calls**	**Total Time** [s]	**Self Time** [s]
BfieldGen	91350	14.805	10.977
@(r,I0)(mu0*I0)./(2*pi*r)	91350	3.593	3.593
Bfield3Phase	15225	8.596	1.235
AmtrGen	6	7.976	0.532
fminsearch	145	0.609	0.364
BfieldGen>@(r,I0)(mu0*I0)./(2*pi*r)	91350	0.235	0.235

In Table A.2 more functions are running, but the 4 most time consuming are the top 5 functions excluding FREQZ which is used to calculate the SNR.

5.3 Hardware

A PCB was constructed with the support of Cadence software, including OrCAD Capture and OrCAD PCB Designer [39]. The cable detection unit's hardware consists of a PCB together with casing and contacts to support various communication protocols and power supply. Figure 5.5(a) and Figure 5.5(b) shows the PCB with its components mounted on both sides. Logic and sensor circuitry are placed on the top of the PCB. Power and interface related electronics are placed on the bottom. The PCB has six copper layers for signal routing and power/ground planes. The design is minimalistic and measures around 8x6 cm.

(a) Top side of the printed circuit board. Microcontroller and sensor circuitry can be seen.

(b) Bottom side of the printed circuit board. Power electronics and communication related circuitry can be seen.

Figure 5.5: The printed circuit board with mounted components. Viewed from top and bottom.

5.4 Measurements

The sensor was placed at five different positions on the test rig and measurements were taken at different heights to verify the functionality. Each position was sampled 4096 times at a sampling rate of 11 kHz. The lab environment where the test rig was set up was the CPAC Systems test lab. The presence of other large current conductors in the lab is unknown but measurements with zero test-rig currents was done to characterize background noise.

5.4.1 Mean Field Strength

Compared to simulations from COMSOL, as seen in Figure 5.6 the results are in the same region. The measurements shows the curved structure of the MFD generated by the conductors. The larger magnitude of measurement of the trefoil formation is explained by the distance between the conductor and the CDU is lesser than the flat formation measurement.

The measurement is deemed to be correct by comparison with simulations. The difference in magnitude between the simulations and the measurement can be explained by the fact that the simulations is described in a perfect environment without the impact of the earth's magnetic field and disturbances sources.

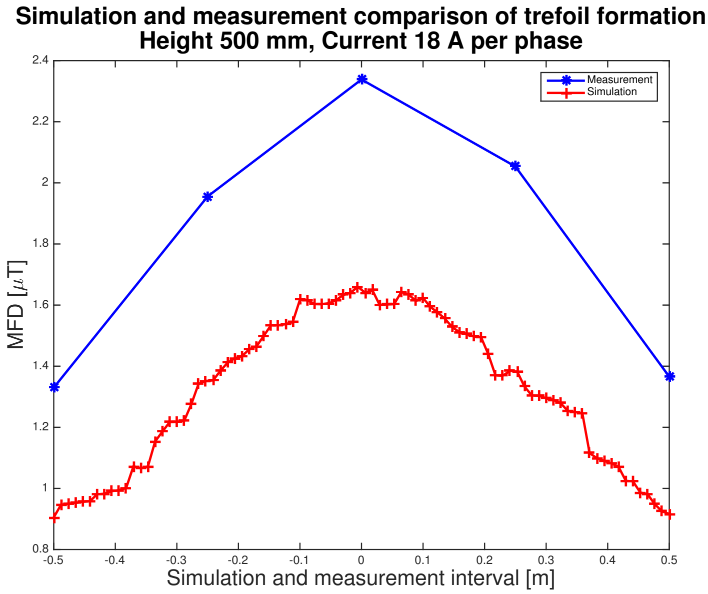

Figure 5.6: Comparison between trefoil measurement and simulations

All measurements show that there is a maximum on a bell-curve-like series of measurements. This max-point can be concluded to be the point closest to the cable. This is true for both trefoil and flat formation cables.

5.4.2 Noise sources

The noise sources that was found in measurements are component noise as described below in this subsection, but also external noise from the lab environment as described in Section 5.4.3. When looking at the FFT of a zero current measurement unexpected and very strong frequencies were discovered. The frequency spectrum in Figure 5.7 has components with high energy levels at 667 and ≈ 1350 Hz. Further analysis led to isolation of the frequency components, and it was discovered that the generation of these frequencies originated from a buck converter on the power supply of the PCB.

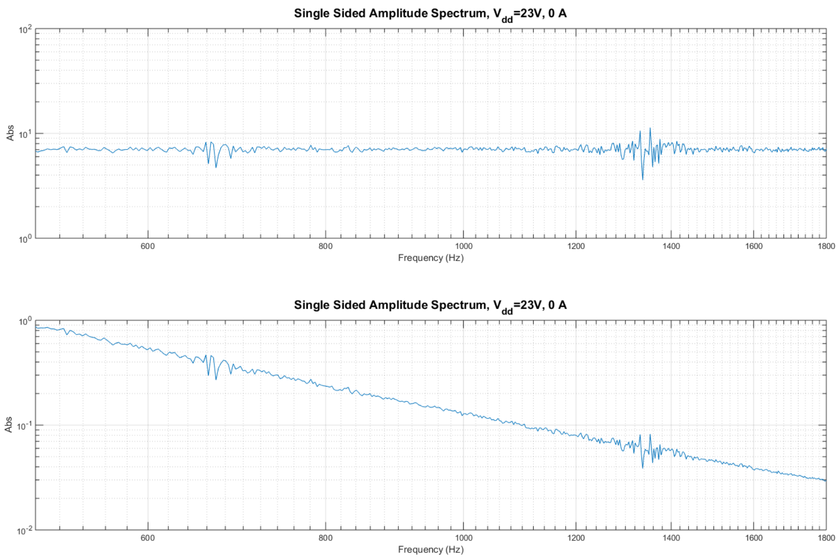

Figure 5.7: The plot on the top shows the unfiltered FFT for $V_{DD} = 23V$. Zoomed in at peaks at 2674 Hz and 4219 Hz. In the plot at the bottom the signal is filtered through a lowpass filter.

The conclusion that the buck converter is the component to create this noise was done by running the system with two different supply voltages, 8 and 23 V. The frequency content differs between the two measurements. A 667 and 1350 Hz signal is present in Figure 5.7 but in Figure 5.8 2674 Hz and 4217 Hz components are present. The measurements were done without prominent current sources around.

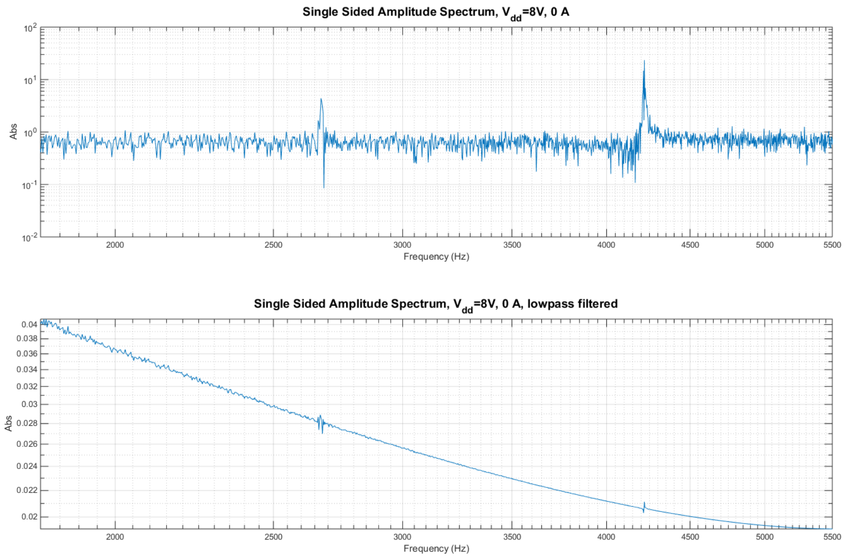

Figure 5.8: The plot on the top shows the unfiltered FFT for $V_{DD} = 8V$. Zoomed in at peaks at 2674 Hz and 4219 Hz. In the plot at the bottom the signal is filtered through a lowpass filter.

5.4.3 FFT

The data was analysed with FFT and the results is presented in Figure 5.9-Figure A.12 and Appendix. A.11-Appendix. A.12. The signal power was specified to multiples of 50 up to 400Hz. The SNR-values are used to be used to distinguish a power cable environment from a non-cable environment. In the zero-current measurements the SNR on our interesting frequencies are 15-37 dB for the flat formation case and 18-36 dB in the trefoil formation case. This will have a huge effect on the SNR values, an effect that was compensated for by removing the zero current frequency energies from the measurements with current. The difference between compensated SNR-values and non-compensated values is obvious while the results still does not correspond with the simulations in Appendix. A.2 and Figure 5.3.

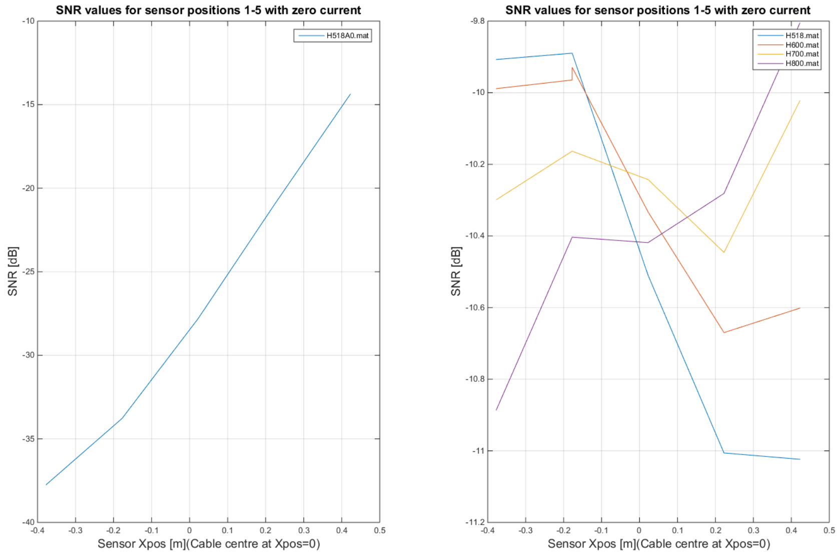

Figure 5.9: The left plot shows the SNR from a measurement with no current with signal power at 50, 100, 150 and 200 Hz. The right plot shows the SNR for different heights and positions. Measurements were performed in flat formation.

5.4.4 Current source reconstruction

As gathered data from the test rig proved reliable the data was fed to the CSR algorithm. The results from the algorithm is shown in Figure 5.11-Figure 5.12 for a sensor height of 700 mm. Plots for all heights are available in Appendix. A.3. All plots have a large overview to the left presenting sensor positions as well as the random point space for each iteration. The coordinate **[0,0]** is the conductor centroid position. To the right a close up is presented. The black point represents the mean point of the last iteration while the red ring represents the standard deviation 1 σ of the last random point space from the mean point.

Results show that the right conductor centroid position can be found within 1 σ of the last iteration mean point when using five iterations. In this case a typical value of σ was 150 mm. Additional iterations yield improved accuracy and σ can be lowered. When running the post-analysis of the data using the CSR-algorithm it was discovered that even if the depth of the cable is not always accurate, the horizontal position most often is less than 1 σ from the horizontal position of the conductor centroid, regardless of the algorithm parameters like convergence-speed and solutions per iteration.

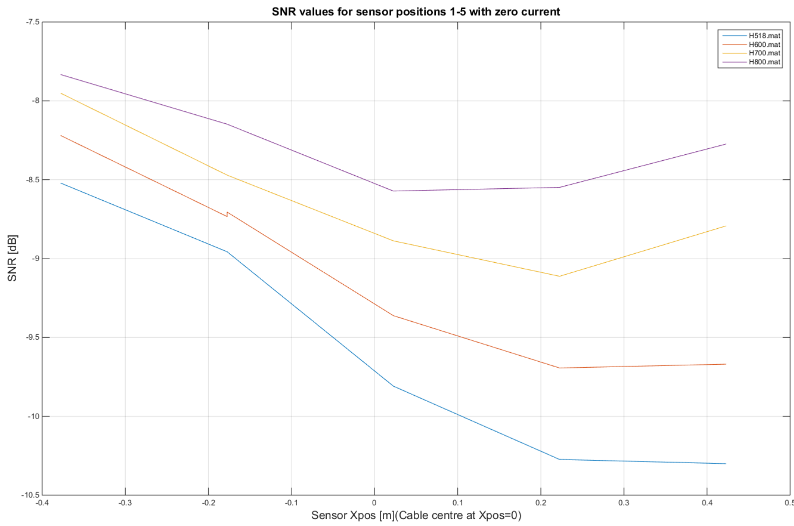

Figure 5.10: The SNR for different heights and positions compensated using the zero-value FFT-data at the lowest height. Measurements were perfomed in flat formation.

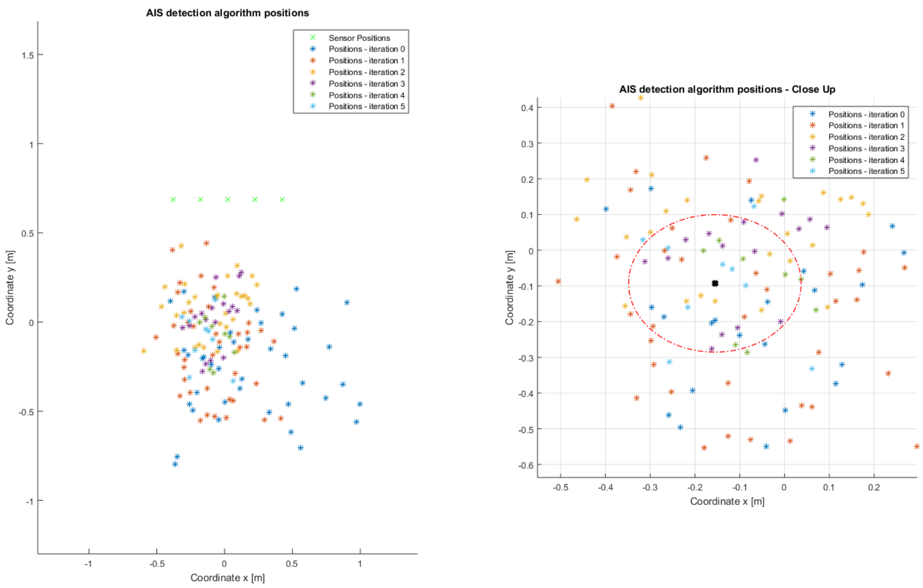

Figure 5.11: Flat cable formation CSR results. Sensors at 700 mm above cable centroid. The approximated current is 13 A. The view is a 2D-coordinate view with depth on the Y-axis and X-axis position on the X-axis. Both are in meters.

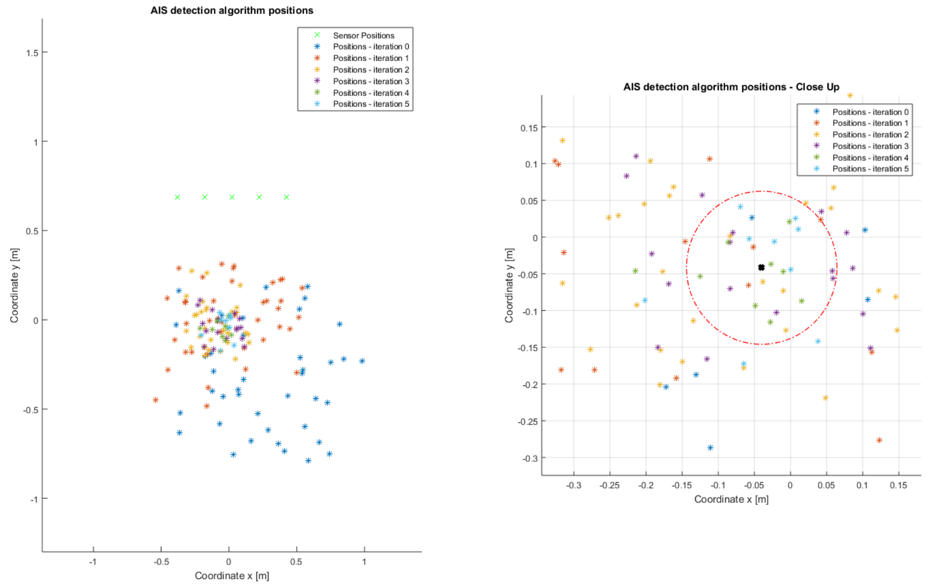

Figure 5.12: Trefoil cable formation AIS results. Sensors at 700 mm above cable centroid. The calculated current is 10 A. The view is a 2D-coordinate view with depth on the Y-axis and X-axis position on the X-axis. Both are in meters.

6
Discussion

The thesis has proven by theory in simulations and also by measurements that it is possible to detect and locate dug down power cables with a passive measurement method. To be able to do this sensitive electronics were designed with focus on noise sensitivity using analog high quality sensors. Processing the data captured by the cable detection unit resulted in both the location of the cable and the current running through it. The design of the cable detection unit was throughout the process done with respect to integration of the sensor network system on the excavator, this was done by designing with respect to a fitting form factor and interfaces such as CAN.

6.1 Software

The software run with measurement data as presented in the results showed that all of the suggested methods worked in their own sense. The mean field strength produced results that are accurate and results did not vary much from the theoretical values. There is a lot of potential to the software part and it could be developed as further testing continues. Some suggestions for higher performance in software is presented in this section.

The quality of solutions would be higher if the position of measurements would have a greater range and/or if the positions would be sampled more dense. To do this with the current platform, the length of a sampling period would have to be shorter and thereby enabling more sampled positions. Since the value was set quite high in the measurements conducted for this report, it can be reduced to meet this requirement.

Based on the results regarding using frequency analysis to detect cables it is concluded that the quantity can tell whether a cable is present. Since the noise in the measurements was higher than the signal, the volatility was not enough to detect any peaks for positions more centered above the cable. To make this possible either the hardware would have to change, or the phase current would have to be higher thus improving the SNR. For suggested hardware changes, see Section 6.2.

The CSR algorithm proved to be competent in finding the cable centroid, but there are many small issues and much uncharted territory. To find the cable position at the low currents used in this lab may be hard, especially for low current trefoil formations. This challenge is due to the low field produced by the low currents, and the CSR performs much better with larger currents and longer distances between sensor and cable. The area around the conductor is much affected by the phase shift in three-phase systems and the field at some distance from the conductor is much more even thus making it more forgiving.

Other challenges with using the AIS-algorithm is the complexity. The strength of the algorithm is randomness, but this is also a fact that obstructs the ability to test different algorithm settings. Many of the parameters for which the algorithm is tweakable are by us unexplored due to time and expertise shortage and a more robust performance could be achieved if these opportunities would be explored. Example of tweak-able parameters are samples per iteration, speed of convergence, number of surviving points per iteration.

The CSR algorithm is tested with 5-6 measurements, but the number of measurements resulting in the best accuracy or performance has not been analyzed. Since the algorithm solves a minimization problem, both its accuracy and computational effort will be higher with more measurements, but a qualified guess is that the accuracy's rate of improvement will stop after 5-6 samples. The minimal number that should be used is three measurements since three measurements can build an arc to fit the models the algorithm is working with. Two points would leave the algorithm unable to guess how close to the conductor the measurements was taken.

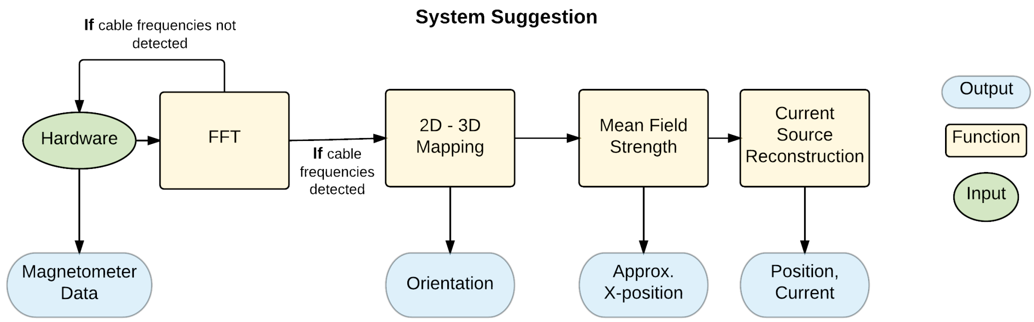

Figure 6.1: A block showing a suggestion for a software system. The blue blocks are outputs, the yellow are functions and the green blocks are inputs.

All of the analyzed post-processing methods have strengths and weaknesses, thus using them together is a good idea. In Figure 6.1 a block diagram for a suggested system is presented. The suggestion based on the result is to start with performing FFT calculations to decide weather a field is present. If these calculations show that there is frequency content on the desired frequencies the mean field strength is used to narrow the search. By finding the max value among the measurements the area at which the cable is situated can be decided more exactly. Narrowing down the search like this will ease the computations having to be done by reducing the iterations or the focus can instead be increased accuracy.

A problem with the CSR algorithm is how many instances needs to be ran. Settings like formation and inter-cable distance will affect the field around the conductor, and the field will be most affected by inter-cable distance for flat formation cables. More research have to go in to what cable types are commonly used in the area of operation. If the probability of a cable type can be concluded and fed into the CDU one could avoid unnecessary calculations and enhance user experience.

6.2 Hardware

The hardware designed in this thesis has worked well and with only small problems. The only real issue that has to be corrected is the buck converter load. The buck converter frequencies discovered in Section 5.4.2 can be moved further out in the frequency spectrum by using a lower input voltage, using more converters connected in series or by matching the load may remove the generation of disturbance frequencies.

To further improve the performance of the software as presented in Table 5.1 and Table A.2 the suggestion is to first put the whole algorithm in C and then analyze what calculations can be moved to the MCU or the Digital signal processing (DSP)-block of the MCU. With AIS-algorithm optimization and moving the algorithm closer to hardware the delay for calculating the conductor position will drop significantly. Using the MCU for calculations improve system performance and reduce delay since the data transferring time can be reduced. The data transferring time is right now the limiting factor for system performance according to logic analyzers.

Another suggestion for increasing performance is to carry out measures to lower the noise floor of the measurements. A lower noise floor would lead to higher volatility for FFT techniques and more accurate AIS positioning. This could be achieved by increasing the sampling rate, changing to a higher resolution ADC or using a dynamic range with the onboard Programmable gain amplifier (PGA). To increase the sampling rate, a different ADC than the one used is needed, and the same solution applies to higher resolution ADC. The best option would be to find a MCU with a better solution ADC. This reduces the communication needed to send the data between units which in turn puts a higher limit for the sampling rate. The other option, using dynamic PGA for the ADC will work only if the offset is not too large and if a way to handle data with dynamic PGA is found.

The MCU's memory bank could also be used more efficiently, offloading the communication interfaces by sending data in larger packets. This could be implemented in software with direct memory access protocol supplied by ST Microelectronics.

6.2.1 Integration

Integration with the existing sensor network solution was not performed. Integration with the existing sensors on the excavator should be used to fuse positioning data of the bucket with data from the CDU. The present interface for communicating with other sensors on the bus is CAN. This will allow us to get accurate position data within a centimeter of the sensor position. The calculations that can not be done on the MCU or its DSP chip can be performed out on a tablet/computer in the cockpit of the excavator.

6.3 Further tests

This thesis had a proof of concept as the purpose. Suggestions for further design is presented, but testing will be a heavy part if the decision is to continue work on the prototype software and hardware. Tests like environmental test described in Section 6.3.1 is obligatory, but to find ways to further develop the present system, more test needs to be carried out.

More lab tests with real cables carrying current would further test the functionality of the prototype. A suggestion is to get in contact with the county land offices and get blueprints to be able to measure on a real cable.

Another aspect that would help make the testing more efficient is to integrate the sensor with data from a inertial measurement sensor before further testing. This would lead to less accuracy demands on the test rig and more flexibility.

The plan for the thesis was to also measure in environments with possibilities for hard/soft iron effects. This has not been done but as a natural progress in the testing of the prototype is mounting it on an excavator arm, this could be tested at the same time.

At last exhaustive testing could be performed by mounting the CDU together with a inertial measurement sensor on a robot and sweep it over the test rig. This test would also lead to more data for analysis which would be useful in further development.

6.3.1 Environmental

During this thesis a lab setup was made, which yielded desired results but a lab area can not simulate the noise and disturbances source that may be found in a live environment. A live environment would also show if the circuitry could be affected by hard/soft iron effects, and therefore further verification of the set/reset functionality that is implemented.

6.4 Ethics and environmental effects

When implemented on a excavator the cable detection unit may save life by detecting cables. The cable detection unit and its passive measurement method provides a safety mechanisms for the operator and personnel on the ground. While the possible destruction of infrastructure has an environmental impact that can be avoided by the cable detection unit.

7
Conclusion

It has been shown in this thesis that it is possible to measure the magnetic flux density of a three phase cable with good accuracy. The common formations of cables could be detected. The accuracy has been proven by the measurement carried out by the custom designed cable detection unit. The cable detection unit measured fields as low as 0.109 μT , while a high-power cable generates MFD at 10-20 μT when measured 1 m away from the conductor.

By using the data gathered together with the CSR algorithm the position and current for the conductors measured could be determined with tolerances at a few centimeters.

The integrational efforts with existing systems was satisfied by supplying interfaces for communication for future integration.

Bibliography

[1] D. K. Cheng and Dawsonera (e-book collection), *Field and wave electromagnetics*. Harlow: Pearson Education, 2014. [Online]. Available: www.summon.com

[2] M. J. Caruso, T. Bratland, C. H. Smith, and R. Schneider, "A new perspective on magnetic field sensing," *SENSORS-PETERBOROUGH-*, vol. 15, pp. 34–47, 1998.

[3] A13ean. (2013) "AMR of permalloy". [Online]. Available: https://commons.wikimedia.org/wiki/File:AMR_of_Permalloy.png

[4] "S. Milano, Allegro MicroSystems, LLC". (2013) Allegro hall-effect sensor ICs. [Online]. Available: http://www.allegromicro.com/en/Design-Center/Technical-Documents/Hall-Effect-Sensor-IC-Publications/Allegro-Hall-Effect-Sensor-ICs.aspx

[5] Nexans, "Mv cable data sheet," Online, 2001, data sheet with 1-core 11 kV cables.

[6] ABB, "XLPE land cable systems users guide," Online, 2010, data sheet of high voltage cables, Rev 5. [Online]. Available: https://library.e.abb.com/public/ab02245fb5b5ec41c12575c4004a76d0/XLPE%20Land%20Cable%20Systems%202GM5007GB%20rev%205.pdf

[7] Nexans, "60-500 kV high voltage underground power cables," Online, 2011, data sheet of high voltage cables. [Online]. Available: http://www.nexans.com/Corporate/2013/60-500_kV_High_Voltage_full_BD2.pdf

[8] PRYSMIAN, "High voltage cables," Online, 2015, data sheet of high voltage cables, Accessed.

[9] "Honeywell international inc.". (2010) 1, 2 and 3 axis magnetic sensors HMC1051/HMC1052L/HMC1053. [Online]. Available: http://www51.honeywell.com/aero/common/documents/myaerospacecatalog-documents/Defense_Brochures-documents/HMC_1051-1052-1053_Data_Sheet.pdf

[10] H. H. Yang, N. Myung, J. Yee, D.-Y. Park, B.-Y. Yoo, M. Schwartz, K. Nobe, and J. W. Judy, "Ferromagnetic micromechanical magnetometer," *Sensors and Actuators A: Physical*, vol. 97, pp. 88–97, 2002.

[11] "Cable Detection Ltd.", 2015. [Online]. Available: http://www.cabledetection.co.uk/

[12] SAE, “The SAE J1939 communications network,” Online, aug 2015, http://www.sae.org/misc/pdfs/J1939.pdf.

[13] M. Engblom, Oskar & Ueda, “Representativa testnät för svenska eldistributionsnät - elforsk rapport 08:42,” Tech. Rep., Juni 2008. [Online]. Available: www.elforsk.se/Rapporter/?download=report&rid=08_42_

[14] "EoN AB Sverige". (2013) Bestämmelser för arbeten nära kablar och elanläggningar. [Online]. Available: https://www.eon.se/privatkund/Kundservice/Grava-nara-ledning/Gravbestammelser/

[15] Leader Cable Industry Berhad. (2015) XLPE insulated power cable. Online.

[16] W. Thomson, “On the electro-dynamic qualities of metals:–effects of magnetization on the electric conductivity of nickel and of iron,” *Proceedings of the Royal Society of London*, vol. 8, pp. 546–550, 1856.

[17] S. A. Macintyre, “The measurement, instrumentation and sensors handbook, chapter magnetic field measurement,” 1999.

[18] M. N. Ali, J. Xiong, S. Flynn, J. Tao, Q. D. Gibson, L. M. Schoop, T. Liang, N. Haldolaarachchige, M. Hirschberger, N. Ong *et al.*, “Large, non-saturating magnetoresistance in wte2,” *Nature*, vol. 514, no. 7521, pp. 205–208, 2014.

[19] E. De Ranieri, A. Rushforth, K. Vỳbornỳ, U. Rana, E. Ahmad, R. Campion, C. Foxon, B. Gallagher, A. Irvine, J. Wunderlich *et al.*, “Lithographically and electrically controlled strain effects on anisotropic magnetoresistance in (Ga, Mn) As,” *New Journal of Physics*, vol. 10, no. 6, p. 065003, 2008.

[20] T. McGuire and R. Potter, “Anisotropic magnetoresistance in ferromagnetic 3d alloys,” *Magnetics, IEEE Transactions on*, vol. 11, no. 4, pp. 1018–1038, 1975.

[21] E. Hirota, H. Sakakima, and K. Inomata, *Giant magneto-resistance devices*. Springer Science & Business Media, 2002, vol. 40.

[22] C. Reig, S. Cardoso, and S. C. Mukhopadhyay, *Giant Magnetoresistance (GMR) Sensors*. Springer, 2013.

[23] E. E. Fullerton and I. K. Schuller, “The 2007 nobel prize in physics: Magnetism and transport at the nanoscale,” *ACS Nano*, vol. 1, no. 5, pp. 384–389, 2007. [Online]. Available: http://dx.doi.org/10.1021/nn700422j

[24] M. N. Baibich, J. M. Broto, A. Fert, F. N. Van Dau, F. Petroff, P. Etienne, G. Creuzet, A. Friederich, and J. Chazelas, “Giant magnetoresistance of (001) fe/(001) cr magnetic superlattices,” *Physical review letters*, vol. 61, no. 21, p. 2472, 1988.

[25] E. Ramsden, “Chapter 1 - hall-effect physics,” in *Hall-Effect Sensors (Second Edition)*, second edition ed., E. Ramsden, Ed. Burlington: Newnes, 2006, pp. 1 – 10. [Online]. Available: http://www.sciencedirect.com/science/article/pii/B9780750679343500028

[26] R. Popovic, P. Drljaca, and C. Schott, “Bridging the gap between AMR, GMR, and Hall magnetic sensors,” in *Microelectronics, 2002. MIEL 2002. 23rd International Conference on*, vol. 1. IEEE, 2002, pp. 55–58.

[27] A. L. Herrera-May, L. A. Aguilera-Cortés, P. J. García-Ramírez, and E. Manjarrez, “Resonant magnetic field sensors based on mems technology,” *Sensors*, vol. 9, no. 10, pp. 7785–7813, 2009.

[28] R. E. Pawinanto, J. Yunas, M. M. Said, M. M. Noor, and B. Y. Majlis, “Design and fabrication of pcb based planar micro-coil for magnetic mems actuator,” in *Semiconductor Electronics (ICSE), 2014 IEEE International Conference on*. IEEE, 2014, pp. 487–490.

[29] P. Di Barba, A. Savini, S. Wiak, and S. (e-book collection), *Field models in electricity and magnetism*. Dordrecht: Springer, 2008.

[30] A. Canova, F. Freschi, M. Repetto, and M. Tartaglia, “Description of power lines by equivalent source system,” *COMPEL - The international journal for computation and mathematics in electrical and electronic engineering*, vol. 24, no. 3, pp. 893–905, 2005.

[31] J. J. Schneider and S. Kirkpatrick, *Stochastic Optimization*. Dordrecht: Springer, 2007.

[32] M. Wahde, *Biologically inspired optimization methods: an introduction*. Southampton: WIT Press, 2008.

[33] L. N. De Castro, F. J. Von Zuben, H. Knidel, L. notes in computer science (e-book collection), S. (e-book collection), and S. O. service), *Artificial immune systems: 6th international conference, ICARIS 2007, Santos, Brazil, August 26-29, 2007 : proceedings*. New York; Berlin: Springer, 2007, vol. 4628.

[34] F. Freschi and M. Repetto, “Comparison of artificial immune systems and genetic algorithms in electrical engineering optimization,” *COMPEL - The international journal for computation and mathematics in electrical and electronic engineering*, vol. 25, no. 4, pp. 792–811, 2006.

[35] D. Schlichthärle, “Oversampling and noise shaping,” in *Digital Filters*. Springer Berlin Heidelberg, 2011, pp. 469–491. [Online]. Available: http://dx.doi.org/10.1007/978-3-642-14325-0_9

[36] "Bur-Brown products, Texas Instruments". (2005) Precision, low power instrumentation amplifiers. [Online]. Available: http://www.ti.com/lit/ds/symlink/ina129.pdf

[37] "STM". (2014) Datasheet - production data. [Online]. Available: http://www.st.com/st-web-ui/static/active/en/resource/technical/document/datasheet/DM00046749.pdf

[38] Texas Instruments. (2011) ADS1258 - 16-channel, 24-bit analog-to-digital converter. Online.

[39] Cadence, "OrCAD Products," Online, Aug 2015, http://www.orcad.com.

A

Appendix

A.1 Sensor data comparison

Table A.1: Sensor data

Manufacturer	Product name	Technology	Range	Sensitivity	Interface	Chip	Fs/Outputrate	Noise
Honeywell	HMC1053	AMR	$\pm 600\mu T$	$mV/V/0.1mT$	Analog	Standalone		$5nV/\sqrt{Hz}$
Honeywell	HMC2003	AMR	$\pm 200\mu T$	$V/0.1mT$	Analog	Module		$29nV/\sqrt{(Hz)}$
Honeywell	HMC5883L	AMR	$\pm 88 to \pm 810\mu T$	$23mT/LSB to 137mT/LSB[16bit]$	I2C	Standalone	160 Hz	$0.2\mu T$
Honeywell	HMC5983	AMR	$\pm 88 to \pm 810\mu T$	$23mT/LSB to 137mT/LSB[16bit]$	I2C,SPI	Standalone	220 Hz	$0.2\mu T$
Freescale	FXMS3110	Unknown	$\pm 1000\mu T$	$0.1\mu T/LSB[16bit]$	I2C	Standalone	80 Hz	$0.25\mu T - RMS$
Freescale	MAG3110	Unknown	$\pm 1000\mu T$	$0.1\mu T/LSB[16bit]$	I2C	Standalone	80 Hz	$0.25\mu T - RMS$
Freescale	FXOS8700CQ	Unknown	$\pm 1200\mu T$	$0.1\mu T/LSB[16bit]$	I2C,SPI	Standalone	800 Hz	$0.3\mu T - RMS$
AKM	AK8963	High sensitive Hall	$\pm 4900\mu T$	$0.15\mu T/LSB[16bit]$	I2C,SPI	Standalone	140 Hz	$Unknown$
AKM	AK8975	High sensitive Hall	$\pm 1200\mu T$	$0.3\mu T/LSB[16bit]$	SPI	Standalone	140 Hz	$Unknown$
ST	LSM303DLHC	AMR	$\pm 130 to \pm 810\mu T$	$90nT/LSB to 434nT/LSB[16bit]$	I2C	Standalone	220 Hz	$Unknown$
ST	LSM303D	AMR	$\pm 200 to \pm 1200\mu T$	$8\mu T/LSB to 8mT/LSB[16bit]$	I2C,SPI	Standalone	100 Hz	$0.6\mu T - RMS$
ST	LIS3MDL	AMR	$\pm 400 to \pm 1600\mu T$	$15nT/LSB to 58.5nT/LSB$	I2C,SPI	Standalone	80 Hz	$0.41\mu T - RMS$
ST	LSM303C	AMR	$\pm 1600\mu T$	$58.5nT/LSB$	I2C,SPI	Standalone	80 Hz	$0.35\mu T - RMS$

A.2 Simulation Results

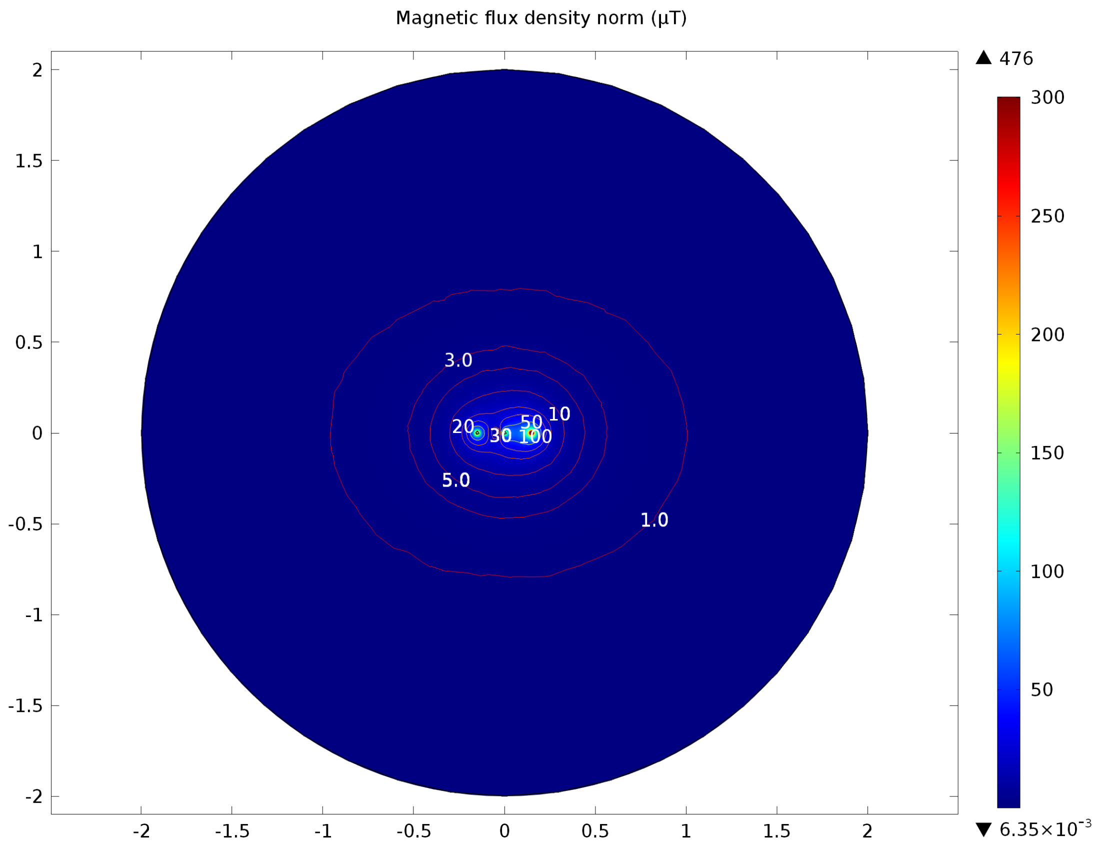

Figure A.1: COMSOL simulation of MFD generated by a 1.5 m long flat formation cable carrying 13 (RMS) A per phase.

A.2.1 FFT

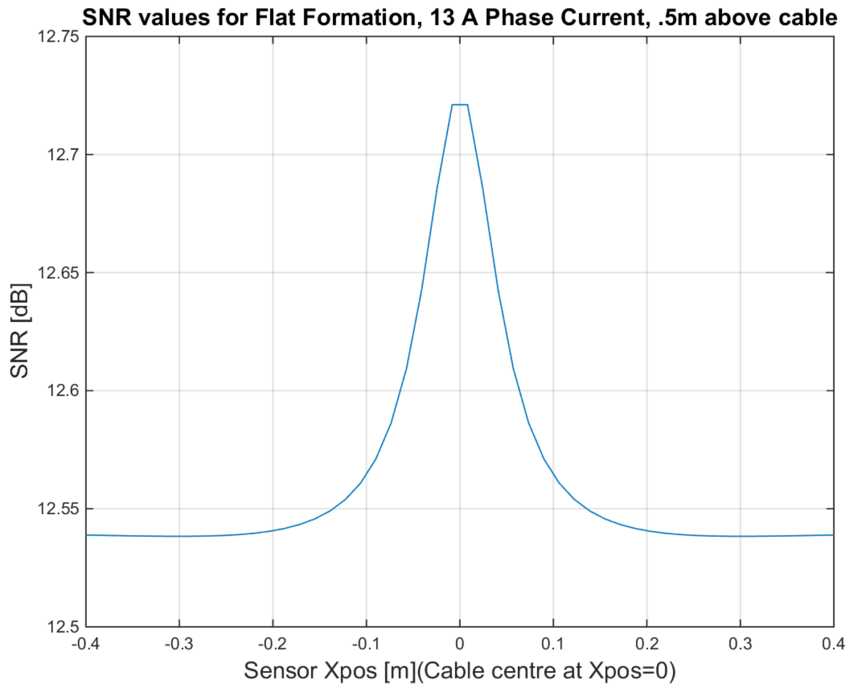

Figure A.2: The FFT for a flat formation cable with 13 A phase current at 0.5 m above the cable centroid.

A.3 AIS plots

All plots have a large overview to the left presenting sensor positions as well as the random point space for each iteration. Coordinate (0,0) is the conductor centroid position. To the right a close up is presented. The black point represents the mean point of the last iteration while the red ring represents 1 σ of the last random point space from the mean point.

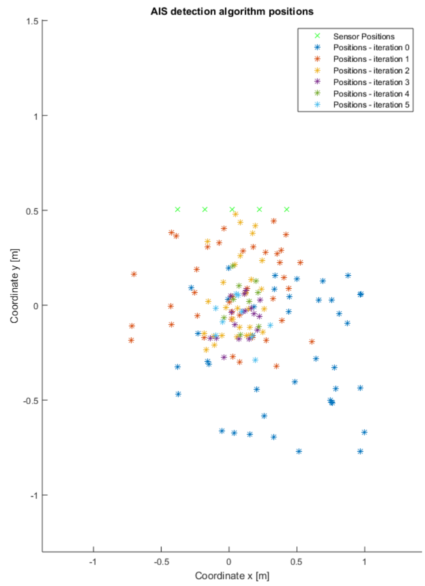

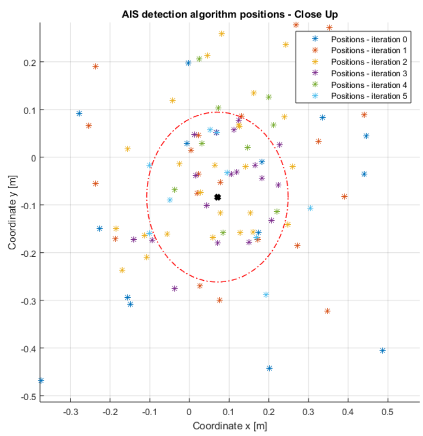

Figure A.3: Flat cable formation AIS results. Sensors at 518mm above cable centroid. The calculated current is 8A.

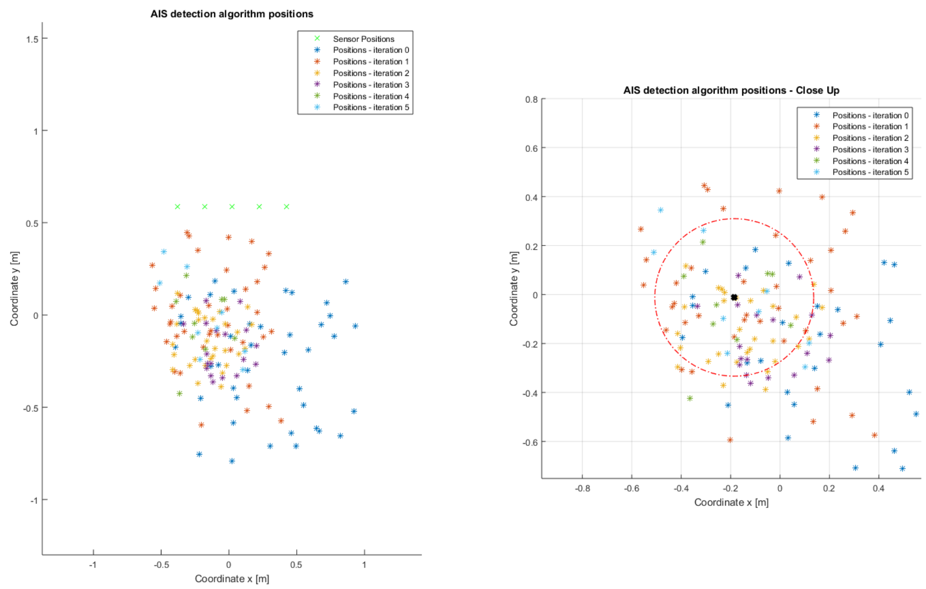

Figure A.4: Flat cable formation AIS results. Sensors at 600mm above cable centroid. The calculated current is 12A.

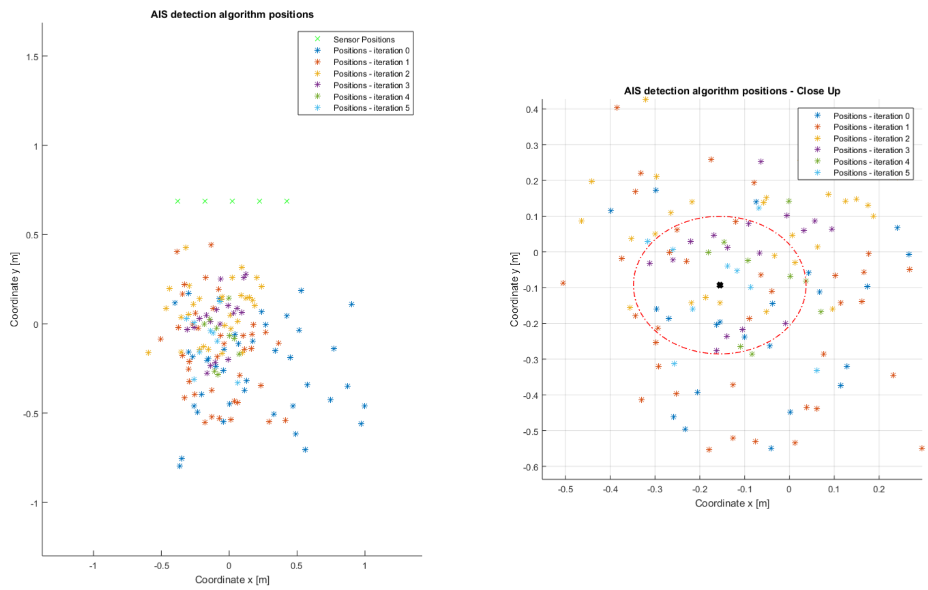

Figure A.5: Flat cable formation AIS results. Sensors at 700mm above cable centroid. The calculated current is 13A.

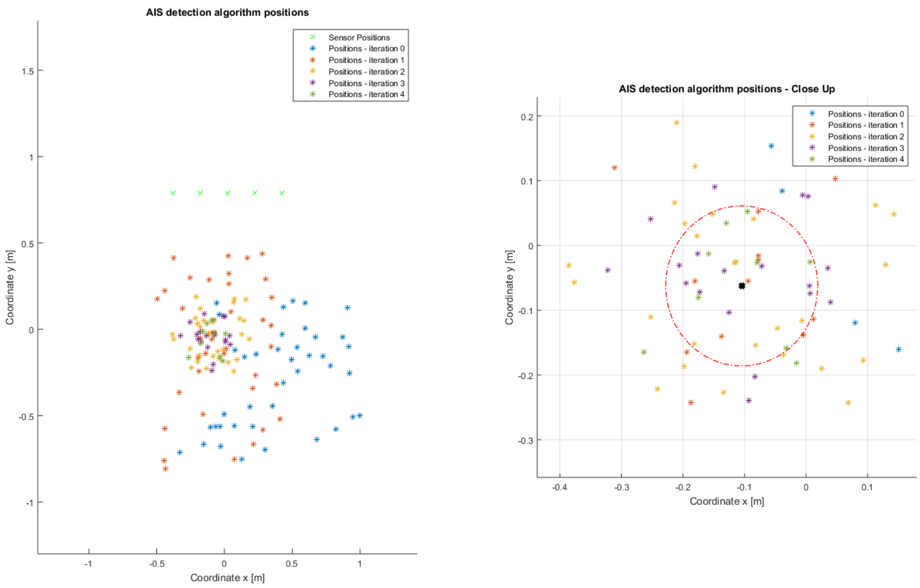

Figure A.6: Flat cable formation AIS results. Sensors at 800mm above cable centroid. The calculated current is 12A.

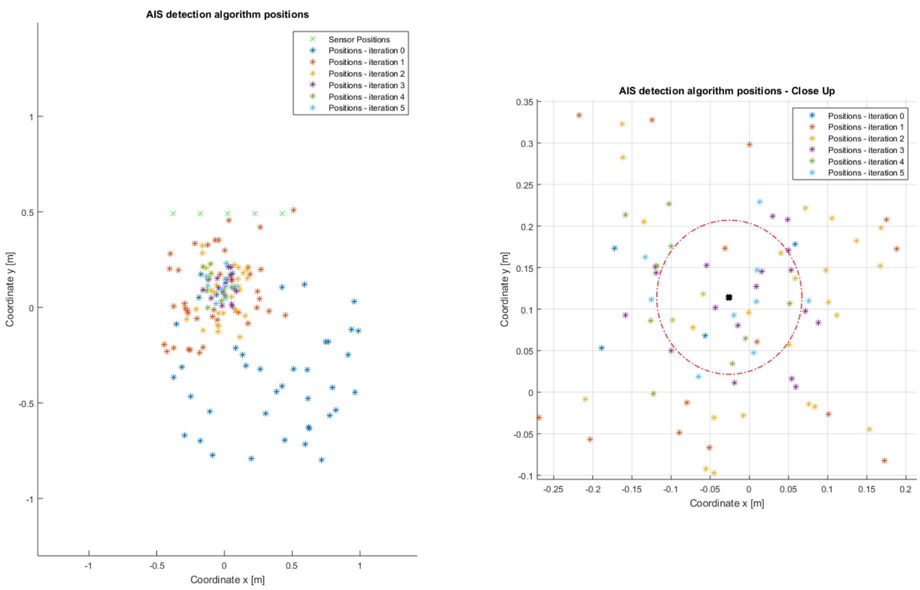

Figure A.7: Trefoil cable formation AIS results. Sensors at 503mm above cable centroid. The calculated current is 15A.

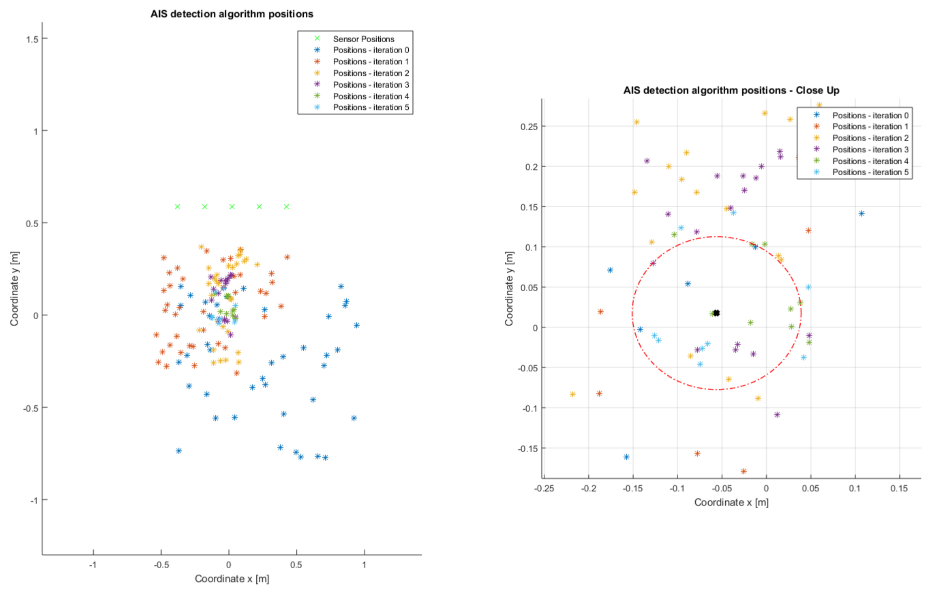

Figure A.8: Trefoil cable formation AIS results. Sensors at 600mm above cable centroid. The calculated current is 10A.

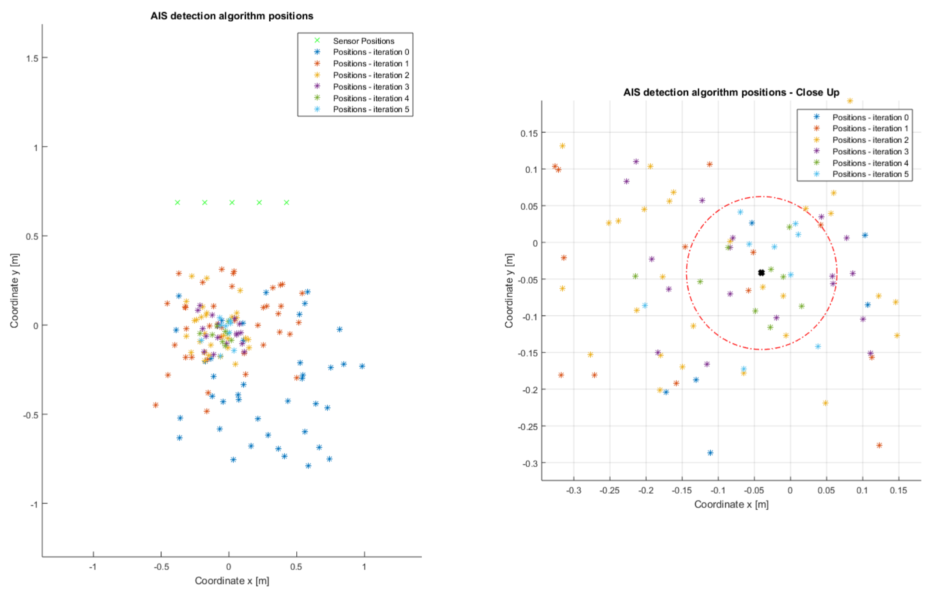

Figure A.9: Trefoil cable formation AIS results. Sensors at 700mm above cable centroid. The calculated current is 10A.

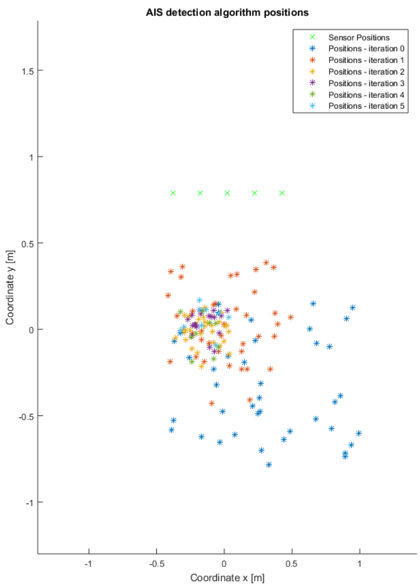

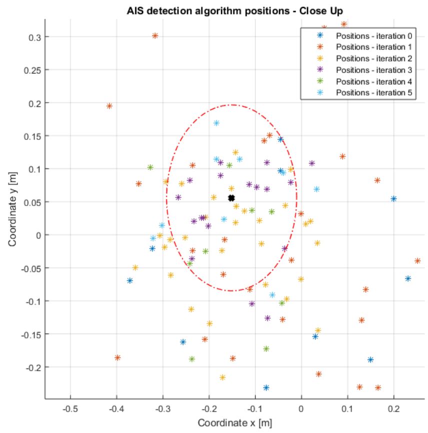

Figure A.10: Trefoil cable formation AIS results. Sensors at 800mm above cable centroid. The calculated current is 10A.

A.4 FFT plots

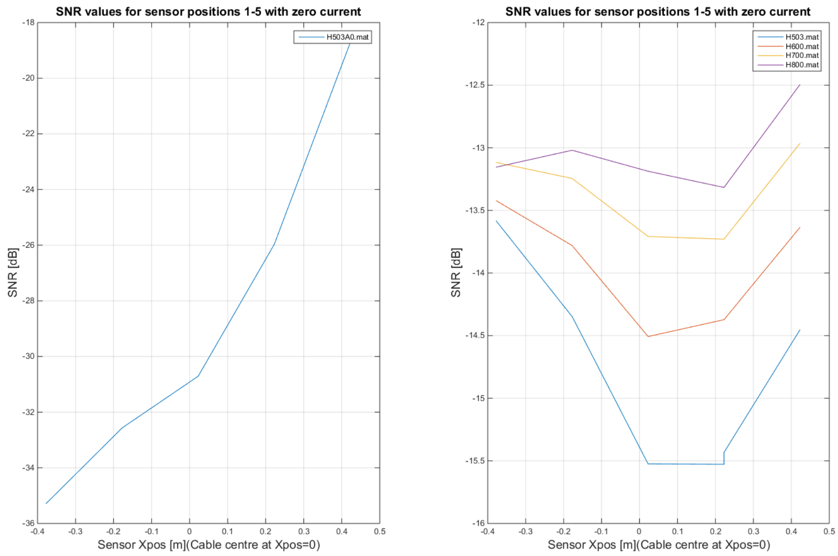

Figure A.11: The left plot shows the SNR for measurement with no current with signal power at 50, 100, 150 and 200 Hz. The right plot shows the SNR for different heights and positions. Measurements were performed trefoil formation.

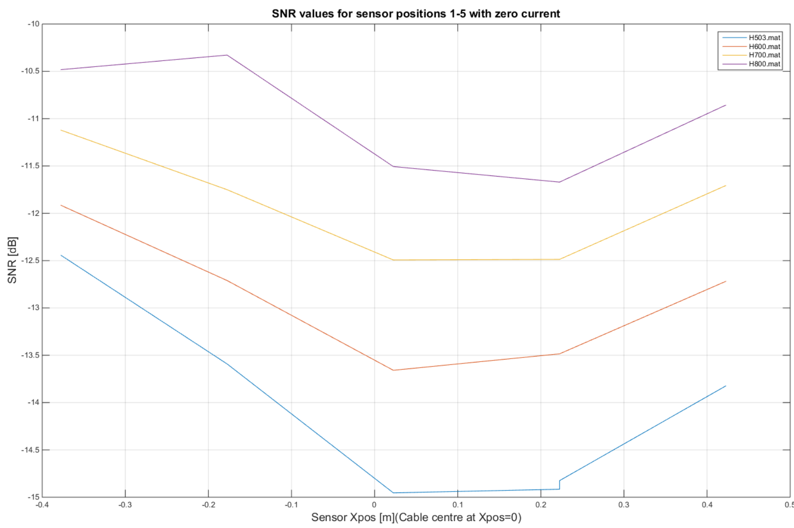

Figure A.12: SNR for different heights and positions compensated using the zero-value FFT data. Measurements were performed in trefoil formation.

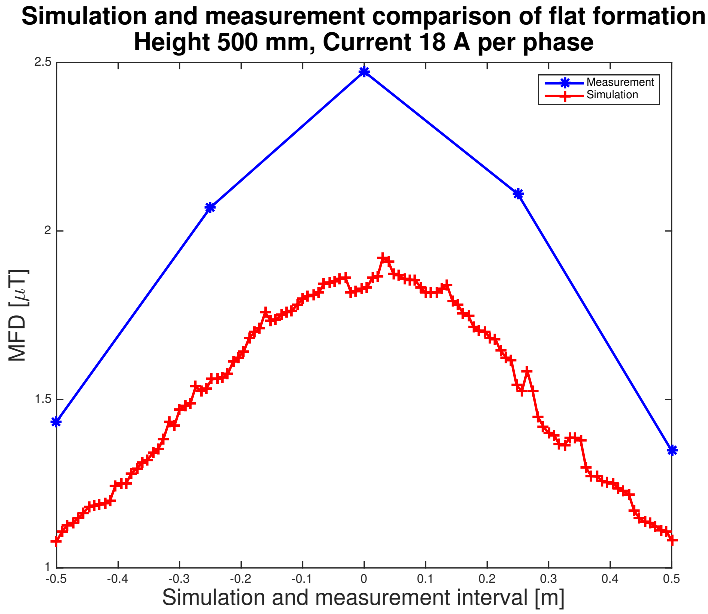

Figure A.13: Comparison between flat measurement and simulations

A.5 Profiling Results

Table A.2: Profiling results from running the FFT-script in matlab. The program was run on an Intel Core i5-3317UM processor. The top 13 time consuming functions are sorted after self-time. The self time is the time the function have been in it self excluding child functions.

Function	**NameCalls**	**Total Time** [s]	**Self Time*** [s]
fspecs.abstractspec.designmethods	3	0.719	0.312
freqz	231	0.425	0.282
dfilt.abstractsos.quantizecoeffs	527	0.499	0.251
firceqrip	1	0.219	0.157
fdesign.abstracttypewspecs.schema	1	0.281	0.156
magFFT	1	5.077	0.139
dfilt.abstractfilter.get_filterquantizer	2515	0.124	0.124
...abstracttypewspecs.updatecurrentspecs	5	0.329	0.110
fdfmethod.abstractcheby1.schema	1	0.313	0.109
dfilt.abstractsos.reorder	24	0.544	0.094
signal	231	0.094	0.094
fmethod.abstractiirwsos.createobj	1	3.015	0.093
dfilt.abstractsos.thissetstates	185	0.094	0.078